



THE UNIVERSITY *of* EDINBURGH

Edinburgh Research Explorer

AN EXPERIMENTAL STUDY OF TRACE ELEMENT FLUXES FROM SUBDUCTED OCEANIC CRUST

Citation for published version:

Carter, LB, Skora, S, Blundy, J, De Hoog, C-J & Elliott, T 2015, 'AN EXPERIMENTAL STUDY OF TRACE ELEMENT FLUXES FROM SUBDUCTED OCEANIC CRUST' *Journal of Petrology*, vol. 56, no. 8, pp. 1585-1606. DOI: 10.1093/petrology/egv046

Digital Object Identifier (DOI):

[10.1093/petrology/egv046](https://doi.org/10.1093/petrology/egv046)

Link:

[Link to publication record in Edinburgh Research Explorer](#)

Document Version:

Early version, also known as pre-print

Published In:

Journal of Petrology

General rights

Copyright for the publications made accessible via the Edinburgh Research Explorer is retained by the author(s) and / or other copyright owners and it is a condition of accessing these publications that users recognise and abide by the legal requirements associated with these rights.

Take down policy

The University of Edinburgh has made every reasonable effort to ensure that Edinburgh Research Explorer content complies with UK legislation. If you believe that the public display of this file breaches copyright please contact openaccess@ed.ac.uk providing details, and we will remove access to the work immediately and investigate your claim.





Draft Manuscript for Review

**AN EXPERIMENTAL STUDY OF TRACE ELEMENT FLUXES
FROM SUBDUCTED OCEANIC CRUST**

Journal:	<i>Journal of Petrology</i>
Manuscript ID:	JPET-Jul-14-0099.R2
Manuscript Type:	Original Manuscript
Date Submitted by the Author:	08-Jul-2015
Complete List of Authors:	Carter, Laura; University Of Bristol, Skora, Susanne; University of Bristol, Earth Sciences Blundy, Jon; University Of Bristol, De Hoog, Jan; University of Edinburgh, School of Geosciences Elliott, Tim; University Of Bristol,
Keyword:	MORB, trace element, experimental petrology, island arc, partial melting, subduction

SCHOLARONE™
Manuscripts

1
2
3 **1 AN EXPERIMENTAL STUDY OF TRACE ELEMENT FLUXES FROM**
4
5
6 **2 SUBDUCTED OCEANIC CRUST**
7
8
9
10
11 **3**
12
13
14
15
16
17
18
19
20
21
22
23
24
25
26
27
28
29
30
31
32
33
34
35
36
37
38
39
40
41
42
43
44
45
46
47
48
49
50
51
52
53
54
55
56
57
58
59
60

Carter, L.B.^{1,2}, Skora, S.^{1,3*}, Blundy, J.¹, De Hoog, J.C.M.⁴, Elliott, T.¹

¹School of Earth Sciences, University of Bristol, Wills Memorial Building, Queen's Road,
Bristol BS8 1RJ, UK

²Department of Earth Sciences, Rice University, 6100 Main Street, Houston, Texas 77005,
USA

³Department Erdwissenschaften, ETH Zürich, Clausiusstrasse 25NW, 8092 Zürich,
Switzerland

⁴School of GeoSciences, University of Edinburgh, Grant Institute, The King's Buildings,
James Hutton Road, Edinburgh EH9 3FE, UKF

*corresponding author: Susanne.Skora@erdw.ethz.ch

Key words: Arc volcanics; experimental petrology; MORB; partial melting; subduction.

ABSTRACT

We have determined experimentally the hydrous phase relations and trace element partitioning behaviour of ocean floor basalt protoliths at pressures and temperatures (3 GPa, 750-1000°C) relevant to melting in subduction zones. To avoid potential complexities associated with trace element doping of starting materials we have used natural, pristine mid-ocean ridge basalt (MORB from Kolbeinsey Ridge) and altered oceanic crust (AOC from DSDP leg 46, ~20°N Atlantic). Approximately 15 wt % water was added to starting materials to simulate fluid fluxing from dehydrating serpentinite underlying the oceanic crust. The vapour-saturated solidus is sensitive to basalt K₂O content, decreasing from 825±25°C in MORB (~0.04 wt % K₂O) to ~750°C in AOC (~0.25 wt % K₂O). Textural evidence indicates that near-solidus fluids are sub-critical in nature. The residual solid assemblage in both MORB and AOC experiments is dominated by garnet and clinopyroxene, with accessory kyanite, epidote, Fe-Ti oxide and rutile (plus quartz/coesite and apatite below the solidus). Trace element analyses of quenched silica-rich melts show a strong temperature dependence of key trace elements. In contrast to the trace element-doped starting materials of previous studies, we do not observe residual allanite. Instead abundant residual epidote provides the host for thorium and light rare earth elements (LREE), preventing LREE from being released ($\Sigma\text{LREE} < 3$ ppm at 750-900°C). Elevated Ba/Th ratios, characteristic of many arc basalts, are found to be generated within a narrow temperature field above the breakdown temperature of phengite, but below exhaustion of epidote. Melts with Ba/Th >1500 and La/Sm_{PUM} (PUM=primitive upper mantle) ~1, most closely matching the geochemical signal of arc lavas worldwide, were generated from AOC at 800-850°C.

47 INTRODUCTION

48 Volcanic arc basalts are widely considered to form from a mantle wedge source region
49 comprising a ternary mixture of hydrous melt from subducted sediment, hydrous fluid (or
50 melt) from (altered) mafic oceanic crust and depleted mantle peridotite (e.g. Elliott, 2003).
51 The distinct trace element chemistry of basalts from different arcs can be ascribed to
52 differing proportions of these three components, reflecting a variation both in inputs to the
53 subduction system and in its thermal structure. Consequently the phase relations of the
54 different subducted components are important to determining under what conditions fluids
55 and melts are generated beneath arcs. If the pressure-temperature dependence of the stability
56 of key residual phases in subducted lithologies can be quantified then potentially the trace
57 element chemistry of arc basalts can be used to infer slab-top temperatures beneath volcanic
58 arcs (e.g. Cooper *et al.*, 2012; Hermann & Spandler, 2008; Klimm *et al.*, 2008; Plank *et al.*,
59 2009). The primary objective of this study is to explore the trace element chemistry of
60 hydrous partial melts associated with ocean floor basalts under subduction zone conditions.

61 Subducted slabs contain H₂O in the form of hydrous minerals, such as amphibole,
62 epidote, micas and serpentine. The breakdown of these minerals during subduction zone
63 metamorphism leads to progressive dehydration of the slab, releasing hydrous fluids into the
64 overlying mantle wedge (e.g. Schmidt & Poli, 1998). If slab temperatures are high enough,
65 as suggested by recent models (e.g. Syracuse *et al.*, 2010; van Keken *et al.*, 2002),
66 dehydration melting of the slab will occur, giving rise to hydrous, silica-rich melts that may
67 similarly ascend into the wedge. Thus both fluid and melt may be extracted from the slab
68 depending on the subduction zone geotherm. If each slab lithology behaves as a closed
69 system during subduction zone metamorphism, the only H₂O available in subducted basalt is

1
2
3 70 that structurally bound in hydrous minerals in the basalt itself. Dehydration melting of such
4
5 71 basalt occurs at relatively high temperatures that may only be achieved where the subducted
6
7
8 72 crust is young and therefore hot. Consequently, there is a long-standing debate as to whether
9
10 73 sub-solidus fluids or supra-solidus hydrous melts are the primary agent of slab-wedge
11
12 74 chemical transfer in subduction zones. Such a simple dichotomy is complicated by the fact
13
14 75 that at sufficiently high pressures silicate melts and hydrous fluids are completely miscible
15
16 76 (above the so-called second critical endpoint) rendering moot any distinction between fluid
17
18 77 and melt. Moreover, the dehydration of serpentine in ultramafic portions of the slab (Ulmer
19
20 78 & Trommsdorff, 1995) may flux overlying basaltic and sedimentary portions with H₂O, such
21
22 79 that dehydration melting of subducted basalt may not be the only melt-producing
23
24 80 mechanism. More in-depth summaries of subduction zone processes can be found in the
25
26 81 recent reviews of Spandler & Pirard (2013) and Schmidt & Poli (2014). Our experiments
27
28 82 were designed explicitly to test this flux-melting mechanism by using starting materials to
29
30 83 which H₂O contents exceeded those that could be contained within hydrous minerals alone.
31
32 84 In that sense our experiments build upon those of Kessel *et al.* (2005a, 2005b), Klimm *et al.*
33
34 85 (2008), Prouteau *et al.* (1999, 2001), and Ryabchikov *et al.* (1996).

35
36
37
38
39
40
41 86 In order to replicate experimentally the phase relations of hydrous ocean floor basalts
42
43 87 it is important to take account of the chemical effects of alteration that occur on the sea floor.
44
45 88 Subducted basalts range in composition from pristine mid-ocean ridge basalts (hereafter
46
47 89 “MORB”), unmodified since eruption, to hydrothermally modified, altered oceanic crust
48
49 90 (hereafter “AOC”) that characterises the upper pillow lavas and sheeted dykes (e.g. Alt *et al.*,
50
51 91 1989). The nature of sea-floor alteration depends on the temperature of hydrothermal
52
53 92 interaction (e.g. Humphris & Thompson, 1978; Mottl, 1983; Thompson, 1983) and, although
54
55
56
57
58
59
60

1
2
3
4 93 its chemical signature is spatially variable, both laterally and vertically (e.g. Kelley *et al.*,
5
6 94 2003), the key chemical changes relative to MORB are an overall rise in alkalis and the
7
8 95 volatile components sulphur, water and carbon dioxide, and to a lesser extent uranium (e.g.
9
10 96 Bach *et al.*, 2003; Gillis & Robinson, 1988; Kelley *et al.*, 2003; Melson, 1968; Mottl, 1983;
11
12 97 Seyfried *et al.*, 1988; Staudigel & Plank, 1996; Staudigel *et al.*, 1981a, 1981b). Previous
13
14 98 experimental studies have attempted to capture this chemical variability by using either
15
16 99 synthetic MORB (e.g. K-free MORB: Kessel *et al.*, 2005a, 2005b; KCMASH: Hermann &
17
18 100 Green, 2001; anhydrous MORB: Yasuda *et al.*, 1994; altered MORB: Klimm *et al.*, 2008;
19
20 101 Ryabchikov *et al.*, 1996) or metamorphosed material (e.g. amphibolite: Kogiso *et al.*, 1997;
21
22 102 Rapp & Watson, 1995; synthetic eclogite: Klemme *et al.*, 2002; Pertermann & Hirschmann,
23
24 103 2003). In several cases the starting materials were doped with trace elements to facilitate
25
26 104 trace element analysis of experimental run products and enhance the stability of accessory
27
28 105 phases (e.g. Klimm *et al.*, 2008). The first aim of our study was to remove the uncertainties
29
30 106 inherent in the use of synthetic and/or trace element-doped starting samples by using natural
31
32 107 ocean floor basalts. The second aim was to explore changes in phase petrology and trace
33
34 108 element partitioning that arises from chemical differences between MORB and AOC.
35
36
37
38
39
40
41
42

110 **METHODS**

111 **Starting Materials**

112 Sample materials used for this study were splits of rock powder that were used for other
113 geochemical studies. The first sample (“MORB”) is a pristine MORB tholeiite (37DS-1)
114 from the Kolbeinsey Ridge, retrieved from 67.08°N, 18.75°W between the Tjörnes and Spar
115 Fracture Zones, at a depth of 170 m (Devey *et al.*, 1994). This sample is extremely fresh and

1
2
3 116 unaltered, though slightly lower in TiO₂ and more depleted compared to average MORB
4
5 117 given in Hofmann (1988, Table 1). Dredged basalts from this site are described as being
6
7 118 mostly glassy with less than 10% (modal) phenocrysts (olivine and minor plagioclase and
8
9 119 spinel for 37DS-1). The fO_2 of MORB is generally around the QFM buffer, amounting to an
10
11 120 average $Fe^{3+}/Fe^{tot} \approx 0.16$ (e.g. Cottrell & Kelley, 2011).
12
13
14

15 121 The second sample (“AOC”) is an altered basalt (15-3, A3, 83-94 cm) from DSDP
16
17 122 leg 46 Hole 396B near the Mid-Atlantic Ridge at a latitude of 23°N and a depth of ~240 m.
18
19 123 This particular horizon is not described in the ODP report, but comes from a massive lava
20
21 124 stream of subunit A3. Other samples from this subunit are described as porphyritic basalts
22
23 125 (approx. 15-25% phenocrysts in leg 46 basalts), containing olivine and plagioclase
24
25 126 phenocrysts with Ca-rich clinopyroxene in the groundmass and spinel. The massive lava is
26
27 127 similar to overlying pillow basalts which can show secondary palagonite, Fe-Mn oxide,
28
29 128 smectite, mica, zeolite and carbonate (e.g. Dungan *et al.*, 1979; Sato *et al.*, 1979). The
30
31 129 seafloor-metasomatised parts of the lava unit exhibit elevated concentrations of H₂O (≈ 2 wt
32
33 130 %), K₂O (≈ 0.3 wt %), Fe₂O₃ ($Fe^{3+}/Fe^{tot} \approx 0.3-0.5$; $fO_2 > QFM$), as well as some other
34
35 131 elements (e.g. S, Rb) (e.g. Dungan *et al.*, 1979). Although carbon is also commonly enriched
36
37 132 in basalts during sea floor alteration, we do not find evidence for significant amounts of CO₂
38
39 133 in our selected samples (a carbonate phase would be expected at least in the sub-solidus
40
41 134 experiment, e.g. Molina & Poli, 2000).
42
43
44
45
46
47

48 135 In Table 1, we compare the major and trace element composition of our starting
49
50 136 materials to average MORB (Hofmann, 1988) and AOC (Kelley *et al.*, 2003), as well as to
51
52 137 some other experimental starting materials to which we later compare our results. A
53
54 138 significant contrast between both starting material compositions is the low K₂O content of
55
56
57
58
59
60

1
2
3 139 MORB (roughly comparable to Kessel *et al.* 2005b) versus the order of magnitude higher
4
5 140 K₂O content of AOC (roughly comparable to that reported by Green & Adam, 2003 and
6
7
8 141 Klimm *et al.*, 2008). Other differences are marked by elevated Na₂O and TiO₂, as well as
9
10 142 reduced MgO contents in the AOC sample.
11
12
13 143

144 **Experimental Techniques**

145 Both starting materials were repeatedly ground with a mortar and pestle and then dried to
146 produce a homogeneous powder. Distilled water (approx. 1.8 µl) was injected into acid-
147 cleaned and annealed Au (T<1000°C) or Au₈₀Pd₂₀ (T≥1000°C) capsules using a Hamilton
148 microsyringe (5 µl). Inaccuracies in injecting small quantities of water are compensated by
149 adjusting the amount of rock powder that is added afterwards such that final H₂O contents
150 were around 15 wt %. The capsules were welded shut using a PUK microwelder. The
151 negligible heating of the welder ensures that H₂O is retained in the capsules, as verified by
152 weighing the water-bearing capsules before and after welding. The experimental cell
153 consisted of inner spacers of crushable alumina, a graphite furnace, outer sleeve of salt and
154 Pyrex, and a W₉₅/Re₅-W₇₅/Re₂₅ (Type “D”), alumina-sheathed axial thermocouple. The
155 friction coefficient for this assembly is 3% (McDade *et al.*, 2002). No account was taken of
156 any pressure effect on thermocouple e.m.f.. Experiments were run in ½-inch, end-loaded
157 piston-cylinder apparatus at the University of Bristol using the ‘hot-piston-in’ method.
158 Experiments were conducted at a pressure (P) of 3 GPa; experimental temperatures (T)
159 ranged between 750-1000°C. The pressure was selected to lie close to the average depth of
160 the Wadati-Benioff zone worldwide (≈105 km, Syracuse & Abers, 2006). Temperatures
161 were selected to bracket the solidus and are in rough agreement with recent thermal models

1
2
3
4 162 of slab-top temperatures beneath arcs (e.g. Cooper *et al.*, 2012; Syracuse *et al.*, 2010; van
5
6 163 Keken *et al.*, 2002). Run durations were 2 to 7 days, in inverse proportion to temperature.
7
8 164 Supra-liquidus runs were carried out at 1.5 GPa and $\geq 1325^\circ\text{C}$ to glass both starting materials
9
10 165 for analysis. Runs were quenched by turning off the power.
11

12
13 166 One experiment was repeated at ETH Zürich after the original showed signs of
14
15 167 disequilibrium (AOC 750°C run, lack of garnet). The same method and furnace assembly
16
17 168 were used, but with a different thermocouple to Bristol (Pt₉₄/Rh₆-Pt₇₀/Rh₃₀; Type “B”). Most
18
19 169 importantly, this run was seeded with 2 wt % of gem quality garnet (composition \approx
20
21 170 Py₅₆Alm₃₇Gross₁Spess₁Andr₅; $< 7 \mu\text{m}$ fraction).
22
23

24
25 171 No attempt was made to control or monitor $f\text{O}_2$. Different pressure-cell assemblies
26
27 172 can lead to variable $f\text{O}_2$ conditions in experiments (e.g., Truckenbrodt *et al.*, 1997), despite
28
29 173 the use of a graphite furnace. For our assembly, in-house estimates of the $f\text{O}_2$ in Bristol lie in
30
31 174 the range NNO+2(± 1) for comparable P-T-time conditions. Conversely, if negligible water is
32
33 175 lost to the assembly, and no iron is lost to the noble metal capsule, the $f\text{O}_2$ is simply a
34
35 176 function of the initial $\text{Fe}^{3+}/\text{Fe}^{\text{tot}}$ (e.g. Kagi *et al.*, 2005). In general, we find that the calculated
36
37 177 ferric iron components in MORB and AOC runs are systematically different, which suggests
38
39 178 that the $f\text{O}_2$ is at least partly controlled by initially different $\text{Fe}^{2+}/\text{Fe}^{3+}$. Since we cannot
40
41 179 exclude that the initial $f\text{O}_2$ was modified during the experimental runs, we consider the initial
42
43 180 bulk $\text{Fe}^{3+}/\text{Fe}^{\text{tot}}$ defines a lower $f\text{O}_2$ limit ($\sim\text{QFM}$ for MORB, $>\text{QFM}$ for AOC, discussed
44
45 181 above), and NNO+2(± 1) an upper limit.
46
47
48
49
50

51 182

52 53 183 **Analytical Techniques**

54
55
56
57
58
59
60

1
2
3 184 Carbon-coated, polished run products were imaged using a Hitachi S-3500N SEM. Major
4
5 185 element electron microprobe analysis (EMPA) was performed in Bristol on a five-
6
7
8 186 spectrometer Cameca SX100, with 15 kV acceleration voltage and 15 nA sample current.
9
10 187 The 750°C repeat experiment was measured at ETH on a five-spectrometer JEOL 8200
11
12 188 Superprobe, using similar conditions. A focused electron beam was used for minerals; for
13
14 189 glasses, a defocused beam, and reduced sample current (4 nA) were used in order to reduce
15
16 190 Na loss, with Na being counted first for 5 seconds only. Due to size issues, a focussed beam
17
18 191 was applied for the quantification of “fish egg” textured spherules (see below), which are
19
20 192 also glassy in nature. These analyses thus likely suffer from loss of volatile elements such as
21
22 193 Na₂O, and concomitant passive enrichment in other major elements.
23
24
25
26

27 194 SIMS analysis of trace elements in experimental glasses was performed at the NERC
28
29 195 facility at the University of Edinburgh using a Cameca IMS-4f ion microprobe. The
30
31 196 following settings were applied: primary beam of 14.5 kV O⁻ ions; 5 nA beam current: ~15
32
33 197 µm diameter beam. NIST SRM 610 glass (Pearce *et al.* 1997) was used to calibrate relative
34
35 198 ion yields; all data were ratioed to Si as determined by EMPA. A 75±20 V energy filter was
36
37 199 applied to positive secondary ions accelerated at 4.5 keV to reduce transmission of molecular
38
39 200 ions. Subsurface inclusions were monitored in a count-rate versus time diagram and
40
41 201 excluded from the averaging procedure. Molecular interferences were removed by
42
43 202 conventional peak-stripping using in-house ION6 software. Matrix-dependent ion-yield
44
45 203 differences between the calibrant (SRM 610) and natural glasses were evaluated by
46
47 204 measuring different standards (MPI DING glasses: STHS, T1, ATHO; USGS glasses: GSD,
48
49 205 BCR, BIR; standard values are taken from GeoRem: <http://georem.mpch-mainz.gwdg.de>)
50
51 206 three times each over 4 days. Calculated Pearson correlation coefficients of calibration
52
53
54
55
56
57
58
59
60

1
2
3 207 curves obtained from these standards are 0.97 or better (see Supplementary Data file 1),
4
5 208 despite the slope of the correlation being offset from unity, similar to what was found by
6
7
8 209 Skora & Bundy (2012). The corrected bulk-rock data measured on the supra-solidus glasses
9
10 210 agree well with trace element data given in Devey *et al.* (1994) for the MORB sample, and
11
12 211 average Leg46, 396B-#3A basalts for the AOC sample (Bougault & Cambon, 1979; Dungan
13
14
15 212 *et al.*, 1979; Emmermann & Puchelt, 1979) (Table 1).

16
17 213 Trace elements in glasses from the repeat experiment (AOC 750°C) were measured
18
19 214 by laser-ablation inductively coupled plasma mass spectrometry (LA-ICP-MS) at ETH
20
21 215 Zürich, using a Resonetics excimer laser (193 nm) coupled to a Thermo Element 2 ICP-MS.
22
23 216 The following settings were applied: spot size = 30 µm; frequency = 5 Hz; fluency = 3.5
24
25 217 J/cm²; acquisition time = 30 s (blank) & 40 s (peak); standards were NIST SRM 612
26
27 218 (external), Ca (internal), GSD-1G (secondary). Data were reduced using the Sills software
28
29 219 (Guillong *et al.*, 2008), and mineral inclusions were excluded from the glass data via
30
31 220 inspection of a count-rate versus time diagram.
32
33
34
35

36 221 To verify the consistency of the SIMS and LA-ICP-MS method we re-analysed all
37
38 222 AOC experiments by LA-ICP-MS. There is general agreement between both datasets to
39
40 223 mostly better than ±20% except for elements with low overall abundances (<0.1 ppm). A
41
42 224 comparison of SIMS and LA-ICP-MS analyses for the supra-liquidus runs is given in
43
44 225 Supplementary Data file 1. In 800-900°C runs where melt segregation was incomplete the
45
46 226 LA-ICP-MS technique encountered problems with numerous sub-surface inclusions. We
47
48 227 therefore prefer to report SIMS data wherever possible. Careful inspection of SIMS and LA-
49
50 228 ICP-MS data further suggested a minor surface contamination of Ba from sample
51
52 229 preparation. Due to the vesicular nature of the glasses, surface contamination can penetrate
53
54
55
56
57
58
59
60

1
2
3
4 230 into the uppermost few μm , which is beyond the sputtering depth of SIMS. For this reason
5
6 231 we report LA-ICP-MS Ba concentrations instead, given that the latter method integrates the
7
8 232 signal from a much greater depth ($\sim 20 \mu\text{m}$).
9

10 233

13 234 **RESULTS**

15 235 **Phase Relations**

17
18 236 All experiments but one (Bristol AOC run at 750°C , no garnet) produced an eclogitic
19
20 237 residual assemblage (garnet, omphacitic clinopyroxene) along with some minor and
21
22 238 accessory phases (e.g. kyanite, epidote, rutile, Fe-Ti oxide). Due to the water-rich nature of
23
24 239 these experiments, all run products contain abundant glass (quenched, supra-solidus melt)
25
26 240 that often exhibit evidence for the presence of a co-existing vapour phase in the form of large
27
28 241 vapour bubbles. These are sometimes decorated with “fish egg” textured spherules, thought
29
30 242 to represent the quenched silicate fraction of a vapour phase rich in dissolved silicates (*c.f.*
31
32 243 Adam *et al.*, 1997, discussed below in more detail). Melt/fluid segregation towards the top of
33
34 244 the capsule occurred in most runs. All phase proportions (Fig. 1 and Table 2) were
35
36 245 determined by least squares regression for average compositions of major phases only,
37
38 246 recalculated on an anhydrous basis. Water is re-integrated into the mass balance at a later
39
40 247 stage (e.g. Klimm *et al.*, 2008). Note that due to the presence of two immiscible fluids
41
42 248 (hydrous melt and siliceous vapour), we cannot calculate the H_2O content of the melt phase,
43
44 249 because the fraction of the vapour phase is unconstrained. Thus the calculated liquid fraction
45
46 250 in Table 2 represents the bulk liquid (melt+vapour), and not just the melt fraction.
47
48
49
50

51
52
53 251 Mineral textures and phase petrology vary slightly between MORB and AOC run
54
55 252 products. Selected SEM images are given in Fig. 2. In general, MORB experiments at 800-
56
57
58
59
60

1
2
3 253 900°C contain phases that tend to be relatively fine-grained (5-20 μm diameter). Garnets are
4
5
6 254 inclusion-poor and chemically homogenous when compared to many other experimental
7
8 255 studies. At 1000°C, in contrast, garnets are relatively coarse grained (20-40 μm), inclusion-
9
10 256 rich and zoned.

11
12
13 257 The sub-solidus MORB experiment (800°C) contains garnet, clinopyroxene, kyanite,
14
15 258 epidote, quartz/coesite, rutile, and abundant vapour (no melt). Neither apatite nor phengite
16
17 259 was observed due to low bulk K_2O and P_2O_5 respectively (Table 1). Glass and additional
18
19 260 garnet replace quartz/coesite, kyanite and some clinopyroxene in the 850°C experiment.
20
21 261 Iron-Ti oxide also appears above the solidus. Importantly, epidote remains present above the
22
23 262 solidus and does not change in composition to allanite (REE-rich epidote-group mineral) as
24
25 263 observed in the doped experiments of Klimm *et al.* (2008). Glasses at 850-900°C exhibit two
26
27 264 distinct types of vesicles: microvesicles (~sub- to 1 μm) and large (~10-100 μm), irregular
28
29 265 vesicles that may or may not contain “fish eggs.” Microvesicles are common in quenched
30
31 266 glasses in water-rich experiments (e.g. Klimm *et al.*, 2008) and are typically ascribed to the
32
33 267 fact that the maximum amount of water that can be quenched into room temperature glasses
34
35 268 is only 8-10 wt.% (e.g. McMillan & Holloway, 1987), whereas the solubility of water in
36
37 269 melts at run conditions is significantly higher (>35 wt % at $P \geq 4$ GPa, e.g. Kessel *et al.*,
38
39 270 2005b). The second, larger set of vesicles is thought to represent a siliceous vapour phase
40
41 271 that co-existed with melt at run conditions, exsolving the silicate fraction upon quench to
42
43 272 form “fish eggs.” At 1000°C epidote and rutile melted out, but a variety of quench crystals
44
45 273 (phengite and other, unidentified, very small phases) are present. In addition, there is no
46
47 274 textural evidence for an additional vapour phase at 1000°C.
48
49
50
51
52
53
54
55
56
57
58
59
60

1
2
3 275 Major phases in AOC run products at 800-1000°C are typically much coarser-grained
4
5 276 (20-80 μm). Minor phases (e.g. rutile, etc.) are fine-grained (5-20 μm). The coarse-grained
6
7
8 277 garnets are often inclusion-rich, and exhibit typical growth zoning. In contrast, the AOC
9
10 278 750°C repeat experiment exhibits many small garnets due to the presence of garnet seeds in
11
12 279 this run (Fig. 2). In clinopyroxenes, we find that omphacitic rims often overgrow smaller,
13
14 280 Na-poor cores, which are likely magmatic relicts, given that their compositions are similar to
15
16 281 those in the ODP report of Sato *et al.* (1979). Igneous clinopyroxenes apparently provided
17
18 282 nuclei for high-pressure experimental clinopyroxenes. Fortunately, relict clinopyroxene
19
20 283 cores in AOC experiments are of minor volumetric abundance compared to their omphacitic
21
22 284 rims.
23
24
25
26

27 285 One AOC experiment (Bristol, 750°C) contains clinopyroxene, staurolite, phengite
28
29 286 epidote, quartz/coesite, rutile, Fe-Ti oxide, apatite and vapour with abundant “fish eggs”.
30
31 287 Garnet and clear evidence for melt are lacking. Repeating this experiment at ETH with
32
33 288 garnet seeds produced abundant garnet, as growth rims (Fig. 2), clinopyroxene, glass and
34
35 289 rutile, as well as fine-grained epidote-clinozoisite; we interpret this repeat run as a more
36
37 290 close approach to equilibrium (see detailed discussion below). Changes in phase
38
39 291 assemblages and proportions are fairly consistent with increasing temperature. Glass, garnet,
40
41 292 clinopyroxene and some trace phases (rutile, Fe-Ti oxide, epidote, kyanite) remain present
42
43 293 up to 900°C. Apatite is either melted out above the solidus or too small to observe. Similar to
44
45 294 MORB experiments, a vesicular glass coexists with an additional fluid phase (large vesicles
46
47 295 with or without fish-eggs) at 750-850°C. The 900°C run product visually differs from the
48
49 296 850°C run product by having a slightly increased glass fraction and no clear evidence for the
50
51
52
53
54
55
56
57
58
59
60

1
2
3 297 second fluid phase. At 1000°C glass, with quench crystals, is abundant (>40%), and epidote,
4
5
6 298 rutile and kyanite are melted-out.
7

8
9 299

10 300 **Approach to equilibrium**

11
12 301 It is straightforward to show that near-equilibrium conditions were reached with our MORB
13
14 302 starting material, which was a glassy basalt with less than 10% olivine and minor plagioclase
15
16
17 303 and spinel. All igneous phases were fully replaced by an eclogitic assemblage (garnet,
18
19 304 clinopyroxene, other minor and accessory phases, as well as melt above the solidus), which
20
21 305 is relatively homogeneous and comparable to other studies (Supplementary Data (SD) file
22
23 306 2). The AOC run products exhibit broadly similar phase assemblages, as well as melt and
24
25 307 mineral compositions that are comparable to MORB run products (SD file 2). This suggests
26
27 308 that near-equilibrium conditions were reached in all but a single Bristol AOC run at 750°C,
28
29 309 which lacked garnet. The failure of garnet to nucleate can be explained by its sluggish
30
31 310 nucleation kinetics in high-pressure experiments. This conclusion is consistent with the
32
33 311 presence of garnet overgrowth rims in the garnet-seeded, repeat experiment at ETH Zürich,
34
35 312 indicating that garnet belongs to the high-pressure sub-solidus assemblage at 3 GPa, 750°C.
36
37 313 Other AOC run products also exhibit some features indicative of local disequilibrium,
38
39 314 including growth zoning in garnet as well as small relict igneous clinopyroxenes that are
40
41 315 surrounded by omphacite. Mass balance and all interpretations below are based on
42
43 316 volumetrically dominant garnet and clinopyroxene rim compositions, because they will be in
44
45 317 equilibrium with the co-existing phases.
46
47
48
49
50
51
52

53 318

54 55 319 **Phase chemistry - major elements**

1
2
3 320 Experimental glasses and silicate minerals are relatively homogenous: in most cases major
4
5 321 elements have 1σ of <10% relative; minor elements have $1\sigma = 10-50\%$ relative (Table 3).
6
7
8 322 Notable exceptions are glasses in the MORB 850°C experiment, hampered because the small
9
10 323 melt pools are not well interconnected, as well as both 1000°C experiments due to the
11
12 324 development of abundant quench crystals. In the latter cases, however, the average of a large
13
14 325 number of analyses should approximate the equilibrium composition, despite large standard
15
16 326 errors. *Glasses* are generally rich in SiO₂, Al₂O₃, CaO and alkalis, and poor in MgO and
17
18 327 FeO. Low EMPA totals as well as the microvesicular nature of quenched glasses imply that
19
20 328 they contain significant H₂O. “Fish egg” textured spherules also appear glassy in nature and
21
22 329 are broadly granitic in composition (see Table 4).
23
24
25
26

27 330 The MORB partial melts are peraluminous and tonalitic in composition (according to
28
29 331 the classification scheme of Barker, 1979) just above the solidus, trending towards a more
30
31 332 metaluminous composition at higher temperatures (Fig. 3). The AOC partial melts are also
32
33 333 peraluminous, but trondhjemitic. Like MORB melts, they become metaluminous at higher
34
35 334 temperatures, and further change their composition at $T \geq 900^\circ\text{C}$ to become tonalitic (Fig. 3).
36
37 335 Magnesium oxide and FeO contents of all glasses are uniformly low, although both elements
38
39 336 increase slightly at higher temperatures (Fig. 4). The Mg# decreases slightly between 750
40
41 337 and 1000°C from around 0.5-0.6 to around 0.4-0.5 in both experimental sequences (Table 3).
42
43 338 Such compositions are fully consistent with other published studies on partial melts of a
44
45 339 basaltic composition with excess water (range: 5-25 wt.%) at broadly similar P-T (Pressure-
46
47 340 Temperature) conditions (e.g. Ryabchikov *et al.*, 1996 (E3 composition); Prouteau *et al.*,
48
49 341 2001 (3 GPa subset); Kessel *et al.*, 2005b (4 GPa, 900-1000°C subset); Klimm *et al.*, 2008;
50
51 342 Prouteau & Scaillet, 2013) (SD file 2). Remaining small discrepancies between all these
52
53
54
55
56
57
58
59
60

1
2
3 343 studies can be related to differences in bulk composition, fO_2 , pressure (range: 2.5-4 GPa)
4
5 344 and the degree of melting as a consequence of different starting H_2O contents.
6
7

8 Major element compositions of minerals are given in SD file 3. The method of Droop
9
10 346 (1987) was used to estimate Fe^{3+} contents for garnet and clinopyroxene and stoichiometric
11
12 347 considerations are used for all other minerals. Garnets in MORB and AOC run products are
13
14 348 compositionally similar at similar temperatures, being rich in almandine (25-40%), pyrope
15
16 349 (30-44%) and grossular (23-30%), but poor in spessartine (<1%) and andradite (1-6%).
17
18 350 Where zoning occurs, garnets display increasing pyrope and decreasing almandine from core
19
20 351 to rim. A small but noticeable difference between the experimental sequences lies in the
21
22 352 calculated andradite component, which tends to be lower at lower temperatures (800-900°C)
23
24 353 in MORB (1-2.7%) than in AOC (1.7-6.5%), in keeping with higher initial Fe^{3+}/Fe^{tot} in
25
26 354 AOC. In contrast, calculated andradite components are consistently higher (5.2-7.5%) at
27
28 355 1000°C. With increasing temperature, the pyrope component increases mostly at the expense
29
30 356 of almandine, gradually changing the Mg# from around 0.4 to around 0.6. Garnet Mg# hence
31
32 357 mirrors the behaviour of melts, which become more iron-rich at higher temperatures. Other
33
34 358 minor elements observed in garnet include TiO_2 , which increases slightly with increasing
35
36 359 temperature in the presence of rutile. Experimental garnet compositions and chemical trends
37
38 360 with temperature are fully consistent with other experimental studies (see SD file 2).
39
40
41
42
43
44
45

46 361 Clinopyroxenes are all omphacites, and are less chemically variable than garnet. A
47
48 362 comparison to other studies is given in SD file 2. They exhibit a significant 'quadrilateral'
49
50 363 (QUAD) Ca-Mg-Fe component (74-76% in MORB, 62-66% in AOC), a jadeite component
51
52 364 (18-24% in MORB, 23-31% in AOC), and a small, but significant, calculated acmite
53
54 365 component (2-8% in MORB, 3-11% in AOC). The acmite component is likely a maximum
55
56
57
58
59
60

1
2
3 366 estimate due to the possible presence of a small Ca-eskolaite component (e.g. Konzett *et al.*,
4
5 367 2007). The relict igneous cores in AOC (750-900°C) are ~90% QUAD in composition, with
6
7
8 368 a relatively high acmite component (4.5-7.5%), and significantly higher Ti compared to
9
10 369 high-pressure, omphacite rims.

11
12
13 370 Minor phases that were observed include kyanite, which is relatively pure Al_2SiO_5 ,
14
15 371 although a small quantity of iron (likely Fe_2O_3) is detectable (~3 wt % in MORB; ~4 wt % in
16
17 372 AOC). Epidotes are epidote-clinzoisite solid solutions, containing approximately 8-10 wt %
18
19 373 total iron, which should be mostly Fe_2O_3 . The SiO_2 phase that occurs in sub-solidus runs
20
21 374 should be coesite, although this is hard to distinguish from quartz in our run products, based
22
23 375 on textural criteria alone. Iron-Ti oxides of the ilmenite-hematite solid solution series are
24
25 376 present in almost all runs, displaying a significant hematite component (~55-75 mol%), and
26
27 377 a small Al_2O_3 component (~1-4 mol%). Rutile, which contains some ferric iron (~2-7
28
29 378 mol%), is present in all runs below 1000°C. Apatite was found in a single run only (750°C;
30
31 379 AOC without melt and garnet), suggesting that this is the main phase that carries P_2O_5 down
32
33 380 to sub-arc depth in phosphate-rich basalts, until it is melted out above the solidus.
34
35
36
37
38
39
40

41 382 **Glass chemistry - trace elements**

42
43 383 With increasing temperature several systematic variations in glass chemistry are observed.
44
45 384 Concentrations are given in Table 5 and plotted (normalised to Primitive Upper Mantle
46
47 385 [PUM]) in Fig. 5 and against temperature in Fig. 6. The AOC experiments provide the most
48
49 386 complete dataset in terms of temperature evolution (750-1000°C), but some insights can also
50
51 387 be derived from the MORB data at 900 and 1000°C. In general, fluid-mobile elements such
52
53 388 as Cs, Rb, Ba, Sr and Li are always enriched in the partial melts. Other elements such as U,
54
55
56
57
58
59
60

1
2
3
4 389 Zr, Hf, and V are also moderately enriched. Elements such as Nb, Ta, LREE and Th are
5
6 390 relatively depleted at $T \leq 900^\circ\text{C}$. Heavy REE, Y and Sc are relatively depleted at all
7
8 391 temperatures. Different element groups behave differently with increasing temperature, e.g.
9
10 392 HREE, Y and Sc concentrations increase with increasing temperature, in contrast to most
11
12 393 fluid-mobile elements. The different trace element patterns are explained in more detail
13
14
15 394 below.

16 17 18 395 19 20 396 **DISCUSSION**

21 22 397 **Location of the Solidus**

23
24 398 Our experiments place constraints on the 3 GPa, H_2O -saturated solidus of ocean floor basalt,
25
26 399 which is shown to be sensitive to bulk K_2O content. Our AOC experiments (~ 0.25 wt.%
27
28 400 K_2O) produced glass (+ garnet, clinopyroxene, minor phases) at 750°C only in the
29
30 401 experiment that contained garnet seeds. The other experiment at 750°C contained “fish eggs”
31
32 402 instead of melt, together with clinopyroxene, staurolite (for reasons detailed in Skora &
33
34 403 Blundy (2010) staurolite is likely metastable relative to garnet and kyanite), phengite,
35
36 404 quartz/coesite and minor phases. It is tempting to conclude that the lack of melt in the latter
37
38 405 750°C experiment is due to garnet nucleation problems and related overall disequilibrium.
39
40 406 However, the most widely proposed H_2O -saturated melting reaction for K-bearing MORB
41
42 407 and sediment is quartz/coesite + phengite + clinopyroxene + H_2O = melt + garnet (e.g.
43
44 408 Hermann & Green, 2001; Hermann & Spandler, 2008; Schmidt, 1996; Skora & Blundy,
45
46 409 2010). As garnet is a product of melting, it is unlikely that the lack of garnet should inhibit
47
48 410 melting. Alternatively, melting in K-bearing AOC may start at temperatures that are very
49
50
51
52
53 411 close to 750°C , and small calibration-related P-T discrepancies between Bristol and ETH
54
55
56
57
58
59
60

1
2
3 412 Zürich (e.g. due to different thermocouple types) may be responsible. For basalt with 0.14
4
5 413 wt.% K₂O and excess water, Lambert & Wyllie (1972) determined a 3 GPa solidus
6
7 414 temperature of ~750°C, whereas Schmidt & Poli (1998) located their solidus at ~730°C for
8
9 415 MORB with 0.49 wt % K₂O. Thus, regardless of whether the lack of melt in one 750°C
10
11 416 experiment is due to P-T uncertainties or due to disequilibrium, we conclude that melting in
12
13 417 K-rich AOC starts at T ≈ 750°C, in keeping with previous studies.
14
15
16

17
18 418 Quenched silicate melt formed only above 800°C in the MORB experiments, placing
19
20 419 the 3 GPa solidus for a starting material with only 0.04 wt.% K₂O between 800 and 850°C
21
22 420 (T=825±25°C). In theory, no phase other than phengite is capable of hosting appreciable
23
24 421 potassium in an eclogitic assemblage at around 3 GPa, a fact confirmed by analyses of
25
26 422 silicate minerals in this run (SD file 3). Sub-solidus phengite, however, was not observed.
27
28 423 Possibly phengites were never found because 0.04 wt % initial K₂O equates to just ~0.4
29
30 424 vol% phengite. Alternatively appreciable potassium was dissolved in the siliceous fluid
31
32 425 (quenched as “fish eggs”) at near-solidus conditions (Table 4), effectively stripping out all
33
34 426 the potassium from the solid assemblage. We note that the K-free, water-rich experiments of
35
36 427 Kessel *et al.* (2005b) determined a 4 GPa solidus temperature of 875±12°C. Assuming a
37
38 428 constant offset between K-bearing and K-free MORB at 3 and 4 GPa, the solidus estimates
39
40 429 of Kessel *et al.* (2005b) and Lambert & Wyllie (1972) can be extrapolated to a 3 GPa, K-free
41
42 430 MORB solidus temperature of around 850°C, consistent with our experimental results. The
43
44 431 melting reaction, however, differs slightly from that given in Kessel *et al.* (2005b). We find
45
46 432 that glass and garnet replace quartz/coesite, kyanite and some clinopyroxene in the 850°C
47
48 433 experiment, suggesting an initially incongruent melting reaction of the form: quartz/coesite +
49
50 434 kyanite + clinopyroxene + H₂O = melt + garnet. Kessel *et al.* (2005b) propose instead a
51
52
53
54
55
56
57
58
59
60

1
2
3 435 congruent melting reaction of the form: clinopyroxene + garnet = melt. To what extent the
4
5
6 436 discrepancies relate to differences in pressure or bulk-rock composition remains uncertain at
7
8 437 this stage, but it is evident that both reactions would occur at somewhat similar temperatures
9
10 438 in subduction zones.

11
12
13 439 The question persists as to whether AOC and MORB can melt at Wadati-Benioff
14
15 440 zone depths (approx. 75-135 km, average \approx 105 km, Syracuse *et al.*, 2010), provided that
16
17 441 sufficient H₂O can be added via the breakdown of hydrous minerals such as serpentine or
18
19 442 chlorite in deeper portions of the slab. Recent results in thermal modelling (e.g. Syracuse *et*
20
21 443 *al.*, 2010; van Keken *et al.*, 2011) predict slab-top temperatures of around 750-850°C in
22
23 444 most subduction zones at 2.5-4.5 GPa (e.g. Lesser Antilles), with some offset towards higher
24
25 445 temperatures (850-950°C, e.g. Nicaragua; Guatemala). These temperatures drop off in the
26
27 446 lower parts of the subducted column, and are approx. 100-300°C lower than slab-top
28
29 447 temperatures at the bottom of a 7 km thick basaltic crust (e.g. van Keken *et al.*, 2011).
30
31 448 Combined with our experimentally-derived, H₂O-saturated solidus temperatures, these
32
33 449 results suggest that only the top part of the basaltic crust can melt, if present as altered
34
35 450 oceanic crust with elevated K₂O contents. K-poor MORB is less likely to melt except in the
36
37 451 hottest subduction zones. Melt fractions of oceanic basalts will be significantly lower
38
39 452 compared to those of overlying, K-rich marine sediments (e.g. Schmidt *et al.*, 2004).
40
41
42
43
44
45
46
47
48
49
50
51
52
53
54
55
56
57
58
59
60

454 **Nature of experimental fluids**

455 The second critical end-point (SCEP) is defined in P-T space by the intersection of the melt-
456 vapour critical curve and the H₂O-saturated solidus (see e.g. Hermann *et al.*, 2006; Manning,
457 2004). The conventional designation of solidus, melt and vapour is lost at pressures
458 exceeding the SCEP because melt and H₂O are fully miscible supercritical fluids.
459 Experimental studies have come to different conclusions concerning the position of the
460 SCEP in the system basalt-H₂O (or more correctly the system basalt-derived partial melt-
461 H₂O). Kessel *et al.* (2005b) used topological criteria to estimate the SCEP in K-free basalt to
462 lie between 5 and 6 GPa. This is close to the position of the SCEP in K-MORB as estimated
463 by Schmidt *et al.* (2004) using textural evidence. On the basis of extrapolation from the
464 haplogranite critical curve to the H₂O-saturated basalt solidus, Klimm *et al.* (2008) proposed
465 that the SCEP lies at ~2.5 GPa in K-MORB. This discrepancy raises the question as to
466 whether MORB/AOC-derived fluids beneath arcs are supercritical in nature, or not.

467 In our experimental charges, MORB glasses at 850-900°C and AOC glasses at 800-
468 850°C clearly exhibit two distinct types of vesicles: (a) microvesicles that are evident in all
469 glass pools and (b) large, irregular vesicles that are also present in glass pools and that may
470 or may not contain “fish eggs.” Microvesicles in glasses (a) are commonly interpreted to
471 represent vapour-exsolution upon quench (e.g. Klimm *et al.*, 2008). Larger vesicles (b) are
472 interpreted to represent an additional vapour phase that co-existed with hydrous melt
473 (=quenched glasses) at run conditions. The “fish eggs” are suggested to represent the
474 siliceous fraction that was dissolved in the vapour phase at run conditions. Our textural
475 evidence argues for two fluid phases at near-solidus conditions, hydrous melt + siliceous
476 vapour (Fig. 7). Our experimental data thus suggest sub-critical conditions and place the

1
2
3 477 SCEP at pressures greater than 3 GPa in both MORB- and AOC-derived fluids, consistent
4
5
6 478 with Kessel *et al.* (2005b) and Schmidt *et al.* (2004). Above 900°C (MORB) and 850°C
7
8 479 (AOC), clear evidence for an additional vapour phase (\pm “fish egg” textured spherules)
9
10 480 disappears, suggesting that complete fluid-melt miscibility (supercritical behaviour) may
11
12 481 occur in response to increasing temperature and changing melt composition. We further offer
13
14 482 a possible explanation for the discrepant result of Klimm *et al.* (2008) in SD file 4.
15
16
17
18 483

19 20 484 **Trace elements in fluid and melt**

21
22 485 It is well known that the behaviour of trace and minor elements in the glass with increasing
23
24 486 temperature is a direct consequence of the residual mineralogy, specifically the phases that
25
26 487 control the budget of those elements (e.g. rutile: Klemme *et al.*, 2002). For elements that
27
28 488 lack a residual host phase the concentration in the glass will decrease with temperature,
29
30 489 whereas for elements with a ubiquitous host phase, element concentrations will increase with
31
32 490 temperature. For elements whose host phase becomes exhausted over the melting interval the
33
34 491 concentration in the glass will attain a maximum at the point of phase exhaustion. Naturally
35
36 492 all trace element contents attain those of the bulk starting material at the liquidus
37
38 493 temperature. A complexity arises for those elements that strongly partition into a separate
39
40 494 vapour phase, i.e. for sub-critical conditions. In that case the exhaustion of the vapour phase
41
42 495 upon attainment of criticality will lead to a maximum in glass concentration in much the
43
44 496 same way as exhaustion of a solid residual phase.

45
46 497 Titanium, Nb and Ta show a continuous increase in concentration with temperature,
47
48 498 with the same trends observed for MORB and AOC, consistent with the persistence of
49
50 499 residual rutile up to 900°C and Fe-Ti-oxide thereafter (Fig. 6). Note that Fe-Ti oxides are
51
52
53
54
55
56
57
58
59
60

1
2
3 500 unlikely to host significant quantities of Nb and Ta because of the significant hematite
4
5 501 component (*c.f.* Skora & Blundy, 2010). In AOC glasses Zr (and Hf) shows a marked peak
6
7 502 in concentration at around 900°C (Fig. 6). We lack the resolution in MORB glasses to
8
9 503 establish if there is a maximum or not. The tendency of Zr and Hf to attain maxima at
10
11 504 intermediate temperatures in AOC suggests the exhaustion of zircon at ~900°C during
12
13 505 melting, although zircon was never positively identified in our experiments due to low bulk
14
15 506 Zr. Scandium, V, Y and HREE also show an overall increase in the glass from 750-1000°C
16
17 507 due to the persistence of garnet and, to a lesser extent, omphacite across the melting interval
18
19 508 (Fig. 6). The slightly complex behaviour of Sc and V may reflect competition between
20
21 509 garnet and omphacite and their changing proportion in the residue with increasing
22
23 510 temperature. Light REE abundances are extremely low (<1-3 ppm total LREE) in all glass-
24
25 511 bearing experiments on MORB and AOC, except at the highest temperature when their
26
27 512 concentrations increase sharply (Fig. 6). This behaviour is a consequence of residual epidote,
28
29 513 which is known to host these elements (e.g. Frei *et al.*, 2004) and approaches exhaustion at
30
31 514 the highest run temperatures. The 800°C AOC run has higher LREE than either of the
32
33 515 adjacent runs. This behaviour is suggestive of less epidote in this run, which may be a result
34
35 516 of a small inter-run variability in fO_2 , which influences epidote stability and proportion
36
37 517 through control of Fe^{3+} . Uranium and Th concentrations are also very low (<0.3 ppm) in all
38
39 518 experimental glasses, and consequently subject to high analytical uncertainty, making trends
40
41 519 hard to discern. Nonetheless Th clearly increases with temperature until $T = 900^\circ C$, similar
42
43 520 to Ce (Fig. 6). Again, epidote appears responsible for this behaviour.
44
45
46
47
48
49
50
51

52
53 521 The LILE K, Ba, Cs, Rb, Sr and Li in glasses show variable behaviour (Fig. 6).
54
55 522 Caesium decreases steadily with temperature in the AOC and MORB experiments,
56
57
58
59
60

1
2
3 523 indicative of behaviour as an incompatible element with no residual host phase. Potassium
4
5
6 524 and Rb show broad maxima at around 800-850°C in AOC, and 900°C (K only) in MORB.
7
8 525 Barium in AOC shows a maximum at 850°C, whereas Li shows a broad maximum at 850-
9
10 526 900°C. Strontium shows a maximum between 900 and 1000°C in both sets of experiments.
11
12 527 Finally, Na shows a maximum in MORB at 900°C, but rather irregular behaviour in AOC.
13
14 528 With the possible exceptions of Sr in epidote (SD file 5) and Na and Li in omphacite (e.g.
15
16 529 Hermann 2002a), none of LILE have a residual host phase; phengite, a potential host for K
17
18 530 and Ba is exhausted above the solidus of MORB and AOC. Thus the maxima that the LILE
19
20 531 display cannot be ascribed to exhaustion of a solid phase. However, it is striking that the
21
22 532 various maxima displayed by LILE roughly correspond to the transition from sub-critical to
23
24 533 super-critical behaviour (850-900°C in AOC, 900-1000°C in MORB), as evidenced
25
26 534 texturally, suggesting a role for fluids in LILE transport. In much the same way as
27
28 535 exhaustion of a solid phase produces maxima for other trace elements so the exhaustion of
29
30 536 the fluid phase on crossing the solvus into super-critical behaviour can lead to maxima in the
31
32 537 concentrations of elements that possibly partition into the fluid. In detail the temperature at
33
34 538 which the maximum occurs over the transition to supercritical behaviour will reflect the
35
36 539 strength of partitioning into the fluid. Thus our data suggest that fluid-melt partitioning
37
38 540 increases in the order Cs<Rb<K<Ba in AOC. The behaviour of Na in this sequence is
39
40 541 unclear. This is an interesting insight into LILE fluid partitioning, but dedicated experiments
41
42 542 would be required to quantify it.
43
44
45
46
47
48
49
50
51 543
52
53
54
55
56
57
58
59
60

544 **Allanite versus epidote and the behaviour of light rare earth elements**

545 The behaviour of LREE+Th in our experimental glasses is controlled by the presence of
546 residual epidote. Light REE abundances are extremely low (<1-3 ppm total LREE, Fig. 8) in
547 all glass-bearing experiments on MORB and AOC, except at the highest temperature when
548 epidote is exhausted. Epidote forms a solid solution with allanite, indicating a demonstrable
549 ability to accommodate LREE in its structure (e.g. Frei *et al.*, 2003). Analyses of epidote in
550 our run products show elevated LREE, in one case readily analysable by EMPA (SD file 5).
551 For example in a run on AOC at 900°C epidote contains 1000±300 ppm Ce, 400±100 ppm
552 La, and 900±300 ppm Nd. The corresponding epidote-melt partition coefficients are:
553 $D_{La} \approx 1500 \pm 600$, $D_{Ce} \approx 1200 \pm 400$, $D_{Nd} \approx 700 \pm 300$ (SD file 6). The observed concentrations of
554 Σ LREE (La-Sm) are much lower than those required for allanite solubility (Fig. 8),
555 confirming that this mineral was absent from our experiments in contrast to those of
556 Hermann (2002a) and Klimm *et al.* (2008). We attribute this key difference to the relatively
557 high doping levels of LREE used in those studies. In fact the LREE partition coefficients
558 between epidote and melt given above are higher than those for allanite at 900°C and 2.5
559 GPa (Klimm *et al.*, 2008) by a factor of ~2.

560 It is logical to conclude that doping with LREE in the experiments of Hermann
561 (2002b), Kessel *et al.* (2005a) and Klimm *et al.* (2008), where allanite was found to be the
562 principal carrier for LREE+Th, simply pushed the composition of the allanite-epidote solid
563 solution to the high LREE end-member, thereby increasing the overall level of LREE+Th in
564 the glasses in the doped experiments. Additional evidence for the stability of allanite versus
565 epidote can be drawn from field examples. Although allanites are found in some (ultra) high-
566 pressure ((U)HP) terrains, they are typically restricted to REE-enriched rocks with alkaline

1
2
3
4 567 affinities (as opposed to N-MORB), or Fe-gabbros (e.g. Hermann, 2002b; Spandler *et al.*,
5
6 568 2003; Tribuzio *et al.*, 1996). These rock types are not representative of average oceanic
7
8 569 basaltic crust and indeed, epidote/zoisite is much more common in exhumed (U)HP terrains
9
10 570 (Enami *et al.*, 2004). Note in that context that UHP terrains most often represent the un-
11
12 571 molten, sub-solidus protolith of subducted crust, and allanite only forms above the solidus
13
14 572 according to Klimm *et al.* (2008) (reaction: epidote = allanite + melt). Our experimental
15
16 573 study suggests however that epidote would not change its composition appreciably above the
17
18 574 solidus.
19
20

21
22 575 We conclude that the control on LREE contents of subduction zone melts of basalt is
23
24 576 still an epidote-group mineral, but one much poorer in LREE than allanite. A simple test of
25
26 577 this proposal is to use the solubility model of Klimm *et al.* (2008), but with the epidote
27
28 578 compositions determined in our experiments (Fig. 7). These have considerably lower mole
29
30 579 fractions of allanite (X_{all}), which leads to much lower levels of LREE in the melt according
31
32 580 to equation (9) in Klimm *et al.* (2008). We use the epidote from the AOC 900°C run with the
33
34 581 LREE contents given in SD file 5. In this run $X_{\text{all}} \approx 0.008$, assuming ideal mixing this would
35
36 582 equate to a LREE content in melts 125 times lower than if pure allanite were present in the
37
38 583 residue. Inspection of Fig. 8 shows that this is indeed the case for this run: at 900°C Klimm
39
40 584 *et al.* (2008) find $X_{\text{all}} \approx 0.4$ and ΣLREE (La-Sm) in the melt is 168 ppm, whereas we have
41
42 585 $X_{\text{all}} = 0.008$ and $\Sigma\text{LREE} = 2.7$ ppm, i.e. X_{all} is 53 times lower and ΣLREE 62 times lower in
43
44 586 our experiment as compared to Klimm *et al.* (2008). The close correspondence between the
45
46 587 observed X_{all} and melt LREE content in our experiments and those of Klimm *et al.* (2008)
47
48 588 lends strong support to the notion that epidote-group minerals limit the flux of LREE from
49
50 589 subducted basalt to the mantle wedge at temperatures below 900°C.
51
52
53
54
55
56
57
58
59
60

1
2
3
4 590 In order to employ the allanite solubility approach to better understand basalt-derived
5
6 591 fluxes of LREE+Th (e.g. Plank *et al.*, 2009), we need a thermodynamic model of the
7
8 592 allanite-epidote solid solution. In addition, we need to constrain the bulk-rock and fO_2
9
10 593 control on epidote-zoisite solid solutions and their respective stability fields. For example,
11
12 594 the stability field of the zoisite end-member in MORB does not extend much beyond 2.5
13
14 595 GPa / 800°C or 3 GPa / 700°C (e.g. Poli *et al.*, 2009; Schmidt & Poli, 1998). Our
15
16 596 experiments reveal that Fe^{3+} -bearing epidote may well be stable at much higher temperatures
17
18 597 at 3 GPa. Hence X_{all} in epidote has the potential to vary significantly. It is also known that
19
20 598 partition coefficients of LREE+Th, and possibly U, vary as a function of the epidote-zoisite
21
22 599 solid solution (see e.g. Frei *et al.*, 2003, 2004; Martin *et al.*, 2011). In the absence of any
23
24 600 such data our experiments provide useful first constraints, demonstrating that negligible
25
26 601 basalt-derived LREE+Th concentrations enter the arc basalt source region. Unless slab-top
27
28 602 temperatures are much higher than existing models would suggest, LREE+Th enrichment in
29
30 603 arc magmas must therefore originate from the sedimentary veneer.
31
32
33
34
35
36
37
38

39 **Implications for arc basalt trace element geochemistry**

40
41 606 Our experiments have a number of implications for the chemistry of the basalt-derived
42
43 607 component added to the mantle wedge source of arc basalts. Although the tripartite model of
44
45 608 the arc magma source reviewed by Elliott (2003) (Fig. 9) advocates an aqueous fluid as the
46
47 609 key-transporting agent of trace elements from the basaltic portion of the slab to the wedge, it
48
49 610 is instructive to evaluate the potential for basalt-derived melts to affect the required chemical
50
51 611 signal. Note that although at super-critical or near super-critical conditions the distinction
52
53 612 between fluid and melt disappears, there is still a relationship between total solutes in the
54
55
56
57
58
59
60

1
2
3
4 613 fluid phase and temperature. At low temperatures, the composition and physical properties
5
6 614 of the fluid phase will resemble an aqueous fluid, whereas at high temperatures it will
7
8 615 resemble a hydrous melt (e.g. Fig. 11 of Hermann & Rubatto, 2014). Thus, our data are
9
10 616 principally also relevant for supercritical fluids that have the physical properties of a hydrous
11
12 617 melt. Our basalt-derived melts approximate the composition of the total subduction
13
14 618 component only in the case of sediment-starved arcs; sediment-derived melts will have quite
15
16 619 different trace element chemistries because of their different bulk compositions, leading to
17
18 620 different residual assemblages at high pressure, and initial trace element inventories. For this
19
20 621 reason we compare directly the trace element composition of our experimental melts to
21
22 622 basaltic arc lavas whose subduction component is thought to be dominated by material from
23
24 623 the mafic crust (e.g. Tonga, Izu-Bonin, some Mariana islands; Elliott, 2003). Since our
25
26 624 experimental starting materials were undoped, it is possible, for the first time, to make direct
27
28 625 inferences about the melt flux from subducted basalt as a function of temperature based on
29
30 626 analyses of trace elements in quenched experimental glasses.
31
32
33
34
35
36
37
38

39 628 *Trace element contribution*

40
41 629 Primitive upper mantle-normalised trace element patterns for melts derived from MORB and
42
43 630 AOC exhibit several striking features (Fig. 5). First, the overall concentrations of trace
44
45 631 elements, relative to PUM, increase with increasing temperature, although fractionation
46
47 632 between adjacent elements decreases with increasing temperature. Thus the most “spiky”
48
49 633 trace element patterns are observed at the lowest temperatures. Second, the only elements
50
51 634 with concentrations significantly higher (factor >3) than PUM at all temperatures, and
52
53 635 therefore able to significantly modify the trace element chemistry of the mantle wedge, are
54
55
56
57
58
59
60

1
2
3 636 the fluid mobile elements (e.g. Cs, Rb, K, Ba, Sr, and U). This is consistent with their
4
5 637 enrichment even in sediment-starved arcs (e.g. Tonga, Izu-Bonin, some Mariana islands).
6
7
8 638 Zirconium, Hf and Li are also surprisingly enriched in our partial melts (see below).
9
10
11 639 Titanium, Nb and Ta enrichments only exceed a factor of 3 at the highest temperatures
12
13 640 studied ($>900^{\circ}\text{C}$). REE are lower than $3\times\text{PUM}$ except at 1000°C .
14

15 641 Sediment-starved arcs typically have low concentrations of many incompatible
16
17 642 elements when compared to sediment-rich arcs, and exhibit low La/Sm, high Ba/Th, as well
18
19
20 643 as Sr isotope ratios consistent with contributions from an altered MORB source. Elliott
21
22 644 (2003) showed that the Ba/Th ratio of the basalt-derived component is in excess of 1000
23
24 645 with a $(\text{La}/\text{Sm})_{\text{PUM}}$ of around 1 (Fig. 5). This special characteristic of the arc geochemical
25
26 646 signature has been traditionally ascribed to a “fluid” phase from subducted mafic oceanic
27
28
29 647 crust. However, similar characteristics are observed in our melts at $800\text{--}850^{\circ}\text{C}$ from an AOC
30
31
32 648 source in which residual epidote is present (retaining Th) but phengite (retaining Ba) is
33
34 649 absent. The same is likely to be true for the 750°C AOC experiment, but exact Ba/Th and
35
36 650 $(\text{La}/\text{Sm})_{\text{PUM}}$ could not be determined because Th, La and Sm were below detection. At
37
38
39 651 higher temperatures the increased Th content, enabled by the progressive breakdown of
40
41 652 epidote, as well as increased melt fractions, reduce Ba/Th significantly (Fig. 5). At lower
42
43 653 (sub-solidus) temperatures, the presence of residual phengite will retain Ba and reduce
44
45
46 654 Ba/Th in the fluid. This is readily apparent from the 650°C , 3 GPa sub-solidus fluid analyses
47
48
49 655 of Green & Adam (2003). At 700°C the Ba/Th of sub-solidus fluids approaches those
50
51 656 measured in our supra-solidus experiments, likely because the solubility of phengite and
52
53 657 other silicates is enhanced in near-solidus fluids (e.g. Manning *et al.*, 2010). (Note in that
54
55 658 context that Green & Adam (2003) used a doped starting material. Whether the absolute
56
57
58
59
60

1
2
3 659 Ba/Th values given in Green & Adam (2003) truly approximate nature requires undoped
4
5
6 660 experiments).

7
8 661 Our results suggest that the Ba/Th and $(La/Sm)_{PUM}$ characteristics of the “fluid”
9
10 662 component can be delivered by a wet melt of basalt (Fig. 9). Further complexity in Ba is
11
12 663 introduced across the transition from sub- to super-critical behavior, as noted above.
13
14 664 However, by far the greatest influence on Ba/Th ratios of melts is the presence or absence of
15
16 665 phengite and epidote. Epidote stability is complex, as discussed above. Phengite stability, in
17
18 666 turn, is primarily a function of bulk K_2O and H_2O , given that there is a strong relationship
19
20 667 between $X_{phengite}$ (the only host of K_2O at sub-arc conditions), H_2O and the degree of melting
21
22 668 (e.g. Schmidt *et al.*, 2004; Skora & Blundy, 2010). In our water-rich experiments, the Ba/Th
23
24 669 ratio of melts supplied by the slab basalt end-member is controlled primarily by temperature,
25
26 670 with the highest ratios being generated in the narrow window between exhaustion of
27
28 671 phengite (at the solidus) and exhaustion of epidote (melted out above the solidus, at approx.
29
30 672 $900^\circ C$). This window lies between $750-800$ and $850^\circ C$ (Fig. 9).
31
32
33
34
35

36 673 It is also worth noting that our sub-solidus, K-poor MORB run product contains
37
38 674 epidote but no phengite, likely because the very low initial potassium content is fully
39
40 675 dissolved in the fluid phase (discussed above). If this is generally the case, then Ba lacks a
41
42 676 host in the sub-solidus mineral assemblage of subducted MORB at these conditions and may
43
44 677 also be concentrated in the fluid phase. In contrast, Th will be retained by residual epidote
45
46 678 and so fluids equilibrated with K-poor MORB at sub-solidus conditions may also have high
47
48 679 Ba/Th ratios. It is therefore conceivable that fluids derived from lower parts of the subducted
49
50 680 basalt, and equilibrated with unaltered MORB at sub-solidus conditions, as well as partial
51
52 681 melt from the uppermost AOC are jointly responsible for the high Ba/Th ratios observed in
53
54
55
56
57
58
59
60

1
2
3 682 sediment starved arcs. Our experiments show how effective epidote can be at keeping Ba/Th
4
5
6 683 high and La/Sm low.

7
8 684 The tendency of our melts to show elevated Zr/Nd (range: 10-1070), Hf/Sm (range:
9
10 685 1-60), and Li/Y (range: 3-80) ratios (Fig. 5) may at first seem paradoxical given that arc
11
12 686 basalts do not show positive anomalies for these elements. Using the same compilation as
13
14
15 687 Elliott (2003) for the most mafic Izu-Bonin and Tonga lavas, these ratios are closer to 7 ± 1
16
17 688 (Zr/Hf), 0.6 ± 0.1 (Hf/Sm) and 0.4 ± 0.1 (Li/Y). However, the trace element ratios of the added
18
19 689 slab component are only mirrored in arc basalts when the elements of interest are not
20
21 690 incorporated significantly into mantle minerals (e.g. Ba/Th). Zirconium, Hf and Li, however,
22
23 691 are only modestly incompatible in mantle minerals (pyroxene, olivine). Studies such as that
24
25 692 of Stolper & Newman (1994) have quantified the exchange of elements with the mantle
26
27 693 wedge and concluded that all but the most incompatible elements are likely to equilibrate
28
29 694 with it. Hence, we suggest that Zr, Hf and Li can be significantly modified by equilibration
30
31 695 with the mantle wedge, to the extent that they no longer provide a clear insight into slab
32
33 696 processes.

34
35
36
37
38
39 697 Finally we note that melts derived from the basaltic portion of the slab have elevated
40
41 698 U/Th ratios. This will lead to isotopic disequilibrium between the activities of ^{238}U and ^{230}Th
42
43 699 that will be retained in the melt on timescales less than five half-lives of ^{230}Th (i.e. 350 ky).
44
45
46 700 An activity excess of ^{238}U over ^{230}Th is a characteristic of many sediment-starved arcs (e.g.
47
48 701 McDermott & Hawkesworth, 1991). For example, in the Marianas the maximum ^{238}U
49
50 702 activity excess over ^{230}Th observed by Elliott *et al.* (1997) and Avanzinelli *et al.* (2012) is
51
52 703 ~ 1.6 (also see Elliott, 2003 for a compilation of high ^{238}U activity excess over ^{230}Th). Such a
53
54 704 value is consistent with basalt-derived melts generated at 800-850°C from AOC, although
55
56
57
58
59
60

1
2
3 705 we note that our source normalized U/Th ratios are poorly constrained due to analytical
4
5 706 limitations.
6
7

8 707

9
10 708 **CONCLUSIONS**

11
12 709 Through a series of experiments conducted at sub-arc P-T conditions (750-1000°C, 3 GPa)
13
14 710 in the presence of excess water, we show that the temperature and composition of the down-
15
16 711 going oceanic crust (pristine MORB versus AOC) can have a profound effect on the sub-arc
17
18 712 phase assemblage and geochemistry, and therefore the resulting slab contribution to arc
19
20 713 magma geochemistry. Notably, an order of magnitude elevated potassium content in AOC
21
22 714 over MORB shifts the water-saturated basaltic solidus to lower temperature (~750°C AOC,
23
24 715 825±25°C MORB). Just above the solidus, run products texturally indicate the presence of
25
26 716 two liquids: an aqueous fluid with quench “fish eggs,” and a vesicular hydrous melt. With
27
28 717 increasing temperature, the second vapour phase diminishes and disappears across the
29
30 718 solvus. Further experimentation at varying P, X_{H_2O} is needed to constrain the solvi and
31
32 719 second critical endpoints for AOC and MORB.
33
34
35
36
37

38
39 720 For slab-top temperature estimates from recent subduction models (e.g. Syracuse *et*
40
41 721 *al.*, 2010), our study confirms the likelihood that melt ± fluid, particularly from an altered
42
43 722 (high-K₂O) oceanic basalt protolith can transport important trace elements to the sources of
44
45 723 arc magmas. Slab-top temperature imparts an important control on trace element
46
47 724 concentrations in the melt and the ratios of key element pairs. In particular, oceanic crust can
48
49 725 contribute melts with high ratios of Ba/Th and U/Th under conditions at which residual
50
51 726 phengite is absent, but epidote is present. The results from our undoped starting materials
52
53
54
55
56
57
58
59
60

1
2
3 727 demonstrate the primacy of residual epidote as opposed to the LREE-rich allanite of
4
5 728 previous, doped experimental studies.
6
7

8 729

9
10 730 **ACKNOWLEDGEMENTS**

11
12 731 This research was based in part on a Masters dissertation by LBC at the University of
13
14 732 Bristol. We thank the workshop at Bristol for assistance with the piston cylinders; S. Kearns
15
16 733 and B. Buse for help with the SEM and EMPA at Bristol; EIMF staff at the University of
17
18 734 Edinburgh for help with SIMS analysis, and M. Guillong for help with the LA-ICP-MS at
19
20 735 ETH. We would like to thank C. Till and an anonymous reviewer for helpful comments on
21
22 736 an earlier version of this paper. The constructive reviews of J G. Prouteau, J. Adam, C.
23
24 737 Spandler, and J Hermann (Editor) have further improved our manuscript, and were greatly
25
26 738 appreciated.
27
28
29
30
31

32 739

33
34 740 **FUNDING**

35
36 741 This work was supported by grants from National Environmental Research Council
37
38 742 [NE/G016615/1], the European Research Council [CRITMAG], and a Wolfson Research
39
40 743 Merit Award to JB, and a Swiss National Science Foundation Ambizione grant
41
42 744 [PZ00P2_142575] to SS.
43
44
45

46 745

47
48 746 **REFERENCES**

49
50
51
52 747 Adam, J., Green, T., Sie, S. & Ryan, C. (1997). Trace element partitioning between aqueous
53 748 fluids, silicate melts and minerals. *European Journal of Mineralogy* **9**, 569–584.
54
55
56
57
58
59
60

- 1
2
3 749 Alt, J., Anderson, T. & Bonnell, L. (1989). The geochemistry of sulfur in a 1.3 km section of
4 750 hydrothermally altered oceanic crust, DSDP Hole 504B. *Geochimica et*
5 751 *Cosmochimica Acta* **53**, 1011–1023.
- 7
8 752 Avanzinelli, R., Prytulak, J., Skora, S., Heumann, A., Koetsier, G. & Elliott, T. (2012).
9 753 Combined ^{238}U – ^{230}Th and ^{235}U – ^{231}Pa constraints on the transport of slab-derived
10 754 material beneath the Mariana Islands. *Geochimica et Cosmochimica Acta* **92**, 308–
11 755 328.
- 13
14 756 Bach, W., Peucker-Ehrenbrink, B., Hart, S. R. & Blusztajn, J. S. (2003). Geochemistry of
15 757 hydrothermally altered oceanic crust: DSDP/ODP Hole 504B - Implications for
16 758 seawater-crust exchange budgets and Sr- and Pb-isotopic evolution of the mantle.
17 759 *Geochemistry, Geophysics, Geosystems* **4**, 1–29.
- 19
20 760 Barker, F. (1979). Trondhjemite: Definition, environment and hypotheses of origin. In:
21 761 Barker, F. (ed.) *Trondhjemites, dacites, and related rocks*. Elsevier, 1–12.
- 22
23 762 Bougault, H. & Cambon, P. (1979). Trace elements: Fractional crystallization and partial
24 763 melting processes, heterogeneity of upper mantle material. *Initial Reports of the Deep*
25 764 *Sea Drilling Project* **46**, 247–251.
- 27
28 765 Cooper, L. B., Ruscitto, D. M., Plank, T., Wallace, P. J., Syracuse, E. M. & Manning, C. E.
29 766 (2012). Global variations in H₂O/Ce: 1. Slab surface temperatures beneath volcanic
30 767 arcs. *Geochemistry, Geophysics, Geosystems* **13**, 1–27.
- 32
33 768 Cottrell, E. & Kelley, K. A. (2011). The oxidation state of Fe in MORB glasses and the
34 769 oxygen fugacity of the upper mantle. *Earth and Planetary Science Letters* **305**, 270–
35 770 282.
- 36
37 771 Devey, C. W., Garbe-Schönberg, C.-D., Stoffers, P., Chauvel, C. & Mertz, D. F. (1994).
38 772 Geochemical effects of dynamic melting beneath ridges: Reconciling major and trace
39 773 element variations in Kolbeinsey (and global) mid-ocean ridge basalt. *Journal of*
40 774 *Geophysical Research* **99**, 9077–9095.
- 42
43 775 Droop, G. (1987). A general equation for estimating Fe³⁺ concentrations in ferromagnesian
44 776 silicates and oxides from microprobe analyses, using stoichiometric criteria.
45 777 *Mineralogical magazine* **51**, 431–435.
- 47
48 778 Dungan, M., Rhodes, J., Long, P., Blanehard, D., Brannon, J. & Rodgers, K. (1979).
49 779 Petrology and geochemistry of basalts from Site 396, Legs 45 and 46. *Initial Reports*
50 780 *of the Deep Sea Drilling Project* **46**, 89–113.
- 52
53 781 Elliott, T. (2003). Geochemical tracers of the slab. In: Eiler, J. (ed.) *Geophysical Monograph*
54 782 *Series 138*. AGU, 23–45.
- 55
56
57
58
59
60

- 1
2
3 783 Elliott, T., Plank, T. & Zindler, A. (1997). Element transport from slab to volcanic front at
4 784 the Mariana arc. *Journal of Geophysical Research* **102**, 14991–15019.
- 5
6
7 785 Emmermann, R. & Puchelt, H. (1979). Abundances of rare earths and other trace elements
8 786 Leg 46 basalts (DSDP). *Initial Reports of the Deep Sea Drilling Project* **46**, 241–245.
- 9
10
11 787 Enami, M., Liou, J. & Mattinson, C. (2004). Epidote minerals in high P/T metamorphic
12 788 terranes: subduction zone and high- to ultrahigh-pressure metamorphism. *Reviews in*
13 789 *Mineralogy and Geochemistry*. AGU **56**, 347–398.
- 14
15
16 790 Frei, D., Liebscher, A., Franz, G. & Dulski, P. (2004). Trace Element Geochemistry of
17 791 Epidote Minerals. *Reviews in Mineralogy and Geochemistry* **56**, 553–605.
- 18
19 792 Frei, D., Liebscher, A., Wittenberg, A. & Shaw, C. S. J. (2003). Crystal chemical controls on
20 793 rare earth element partitioning between epidote-group minerals and melts: an
21 794 experimental and theoretical study. *Contributions to Mineralogy and Petrology* **146**,
22 795 192–204.
- 23
24
25 796 Gillis, K. & Robinson, P. (1988). Distribution of alteration zones in the upper oceanic crust.
26 797 *Geology* **16**, 262–266.
- 27
28 798 Green, T. H. & Adam, J. (2003). Experimentally-determined trace element characteristics of
29 799 aqueous fluid from partially dehydrated mafic oceanic crust at 3.0 GPa, 650–700°C.
30 800 *European Journal of Mineralogy* **15**, 815–830.
- 31
32
33 801 Guillong, M., Meier, D. L. Allan, M. M., Heinrich, C. A. & Yardley, B. W. D. (2008).
34 802 SILLS: A MATLAB-based program for the reduction of laser ablation ICP-MS data
35 803 of homogenous materials and inclusions. *Mineralogical Association of Canada Short*
36 804 *Course* **40**, 328–333.
- 37
38
39 805 Hermann, J. (2002a). Allanite: thorium and light rare earth element carrier in subducted
40 806 crust. *Chemical Geology* **192**, 289–306.
- 41
42
43 807 Hermann, J. (2002b). Experimental constraints on phase relations in subducted continental
44 808 crust. *Contributions to Mineralogy and Petrology* **143**, 219–235.
- 45
46
47 809 Hermann, J. & Green, D. H. (2001). Experimental constraints on high pressure melting in
48 810 subducted crust. *Earth and Planetary Science Letters* **188**, 149–168.
- 49
50
51 811 Hermann, J. & Rubatto, D. (2014). Subduction of Continental Crust to Mantle Depth:
52 812 Geochemistry of Ultrahigh-Pressure Rocks. In: Rudnick, R. L. (ed.) *Treatise on*
53 813 *Geochemistry (Second Edition) 4: The Crust*. Elsevier, 309–340.
- 54
55
56 814 Hermann, J., Spandler, C., Hack, A. & Korsakov, A. (2006). Aqueous fluids and hydrous
57 815 melts in high-pressure and ultra-high pressure rocks: Implications for element
58 816 transfer in subduction zones. *Lithos* **92**, 399–417.

- 1
2
3 817 Hermann, J. & Spandler, C. J. (2008). Sediment Melts at Sub-arc Depths: an Experimental
4 818 Study. *Journal of Petrology* **49**, 717–740.
5
6
7 819 Hofmann, A. W. (1988). Chemical differentiation of the Earth: the relationship between
8 820 mantle, continental crust, and oceanic crust. *Earth and Planetary Science Letters* **90**,
9 821 297–314.
10
11 822 Humphris, S. & Thompson, G. (1978). Hydrothermal alteration of oceanic basalts by
12 823 seawater. *Geochimica et Cosmochimica Acta* **42**, 107–125.
13
14
15 824 Kagi, R., Muntener, O., Ulmer, P. & Ottolini, L. (2005). Piston-cylinder experiments on
16 825 H₂O undersaturated Fe-bearing systems: An experimental setup approaching fO₂
17 826 conditions of natural calc-alkaline magmas. *American Mineralogist* **90**, 708–717.
18
19
20 827 Kelley, K. A., Plank, T., Ludden, J. & Staudigel, H. (2003). Composition of altered oceanic
21 828 crust at ODP Sites 801 and 1149. *Geochemistry, Geophysics, Geosystems* **4**, 1–21.
22
23
24 829 Kessel, R., Schmidt, M. W., Ulmer, P. & Pettke, T. (2005a). Trace element signature of
25 830 subduction-zone fluids, melts and supercritical liquids at 120–180 km depth. *Nature*
26 831 **437**, 724–7.
27
28 832 Kessel, R., Ulmer, P., Pettke, T., Schmidt, M. W. & Thompson, A. B. (2005b). The water –
29 833 basalt system at 4 to 6 GPa : Phase relations and second critical endpoint in a K-free
30 834 eclogite at 700 to 1400°C. **237**, 873–892.
31
32
33 835 Klemme, S., Blundy, J. & Wood, B. (2002). Experimental constraints on major and trace
34 836 element partitioning during partial melting of eclogite. *Geochimica et Cosmochimica*
35 837 *Acta* **66**, 3109–3123.
36
37
38 838 Klimm, K., Blundy, J. D. & Green, T. H. (2008). Trace Element Partitioning and Accessory
39 839 Phase Saturation during H₂O-Saturated Melting of Basalt with Implications for
40 840 Subduction Zone Chemical Fluxes. *Journal of Petrology* **49**, 523–553.
41
42
43 841 Kogiso, T., Tatsumi, Y. & Nakano, S. (1997). Trace element transport during dehydration
44 842 processes in the subducted oceanic crust: 1. Experiments and implications for the
45 843 origin of ocean island basalts. *Earth and Planetary Science Letters* **148**, 193–205.
46
47
48 844 Konzett, J., Frost, D. J., Proyer, A. & Ulmer, P. (2007). The Ca-Eskola component in
49 845 eclogitic clinopyroxene as a function of pressure, temperature and bulk composition:
50 846 an experimental study to 15 GPa with possible implications for the formation of
51 847 oriented SiO₂-inclusions in omphacite. *Contributions to Mineralogy and Petrology*
52 848 **155**, 215–228.
53
54
55 849 Lambert, I. & Wyllie, P. (1972). Melting of gabbro (quartz eclogite) with excess water to 35
56 850 kilobars, with geological applications. *The Journal of Geology* **80**, 693–708.
57
58
59
60

- 1
2
3 851 Manning, C. (2004). The chemistry of subduction-zone fluids. *Earth and Planetary Science*
4 852 *Letters* **223**, 1–16.
- 5
6
7 853 Manning, C. E., Antignano, A. & Lin, H. A. (2010). Premelting polymerization of crustal
8 854 and mantle fluids, as indicated by the solubility of albite+paragonite+quartz in H₂O
9 855 at 1 GPa and 350–620°C. *Earth and Planetary Science Letters* **292**, 325–336.
- 10
11
12 856 Martin, L. A. J., Wood, B. J., Turner, S. & Rushmer, T. (2011). Experimental Measurements
13 857 of Trace Element Partitioning Between Lawsonite, Zoisite and Fluid and their
14 858 Implication for the Composition of Arc Magmas. *Journal of Petrology* **52**, 1049–
15 859 1075.
- 16
17
18 860 McDade, P., Wood, B. J., Van Westrenen, W., Brooker, R., Gudmundsson, G., Soulard, H.,
19 861 Najorka, J. & Blundy, J. (2002). Pressure corrections for a selection of piston-
20 862 cylinder cell assemblies. *Mineralogical Magazine* **66**, 1021–1028.
- 21
22
23 863 McDermott, F. & Hawkesworth, C. (1991). Th, Pb, and Sr isotope variations in young island
24 864 arc volcanics and oceanic sediments. *Earth and Planetary Science Letters* **104**, 1–15.
- 25
26
27 865 McMillan, P. F. & Holloway, J. R. (1987). Water solubility in aluminosilicate melts.
28 866 *Contributions to Mineralogy and Petrology* **97**, 320–332.
- 29
30
31 867 Melson, W. (1968). Volcanism and metamorphism in the Mid Atlantic Ridge, 22° N latitude.
32 868 *Journal of Geophysical Research* **73**, 5925–5941.
- 33
34
35 869 Molina, J. & Poli, S. (2000). Carbonate stability and fluid composition in subducted oceanic
36 870 crust: an experimental study on H₂O-CO₂-bearing basalts. *Earth and Planetary*
37 871 *Science Letters* **176**, 295–310.
- 38
39
40
41 872 Mottl, M. (1983). Metabasalts, axial hot springs, and the structure of hydrothermal systems
42 873 at mid-ocean ridges. *Geological Society of America Bulletin* **94**, 161–180.
- 43
44
45 874 Pearce, N. J. G., Perkins, W. T., Westgate, J. A., Gorton, M. P., Jackson, S. E., Neal, C. R. &
46 875 Chenery, S. P. (1997). A compilation of new and published major and trace element
47 876 data for NIST SRM 610 and NIST SRM 612 glass reference materials. *Geostandards*
48 877 *Newsletter* **21**, 115–144.
- 49
50
51 878 Pertermann, M. & Hirschmann, M. M. (2003). Anhydrous Partial Melting Experiments on
52 879 MORB-like Eclogite: Phase Relations, Phase Compositions and Mineral-Melt
53 880 Partitioning of Major Elements at 2–3 GPa. *Journal of Petrology* **44**, 2173–2201.
- 54
55
56
57
58
59 881 Plank, T., Cooper, L. B. & Manning, C. E. (2009). Emerging geothermometers for
60 882 estimating slab surface temperatures. *Nature Geoscience* **2**, 611–615.

- 1
2
3 883 Poli, S., Franzolin, E., Fumagalli, P. & Crottini, A. (2009). The transport of carbon and
4 884 hydrogen in subducted oceanic crust: An experimental study to 5 GPa. *Earth and*
5 885 *Planetary Science Letters* **278**, 350–360.
- 6
7
8 886 Prouteau, G. & Scaillet, B. (2012). Experimental Constraints on Sulphur Behaviour in
9 887 Subduction Zones: Implications for TTG and Adakite Production and the Global
10 888 Sulphur Cycle since the Archean. *Journal of Petrology* **54**, 183–213.
- 11
12
13 889 Prouteau, G., Scaillet, B., Pichavant, M. & Maury, R. (1999). Fluid-present melting of
14 890 oceanic crust in subduction zones. *Geology* **27**, 1111–1114.
- 15
16 891 Prouteau, G., Scaillet, B., Pichavant, M. & Maury, R. (2001). Evidence for mantle
17 892 metasomatism by hydrous silicic melts derived from subducted oceanic crust. *Nature*
18 893 **410**, 197–200.
- 19
20
21 894 Rapp, R. P. & Watson, E. B. (1995). Dehydration Melting of Metabasalt at 8-32 kbar:
22 895 Implications for Continental Growth and Crust-Mantle Recycling. *Journal of*
23 896 *Petrology* **36**, 891–931.
- 24
25
26 897 Ryabchikov, I. D., Miller, C. & Mirwald, P. W. (1996). Composition of hydrous melts in
27 898 equilibrium with quartz eclogites. *Mineralogy and Petrology* **58**, 101–110.
- 28
29 899 Sato, H., Aoki, K.-I., Okamoto, K. & Fujita, B.-Y. (1979). Petrology and chemistry of
30 900 basaltic rocks from hole 396B, IPOD/DSDP leg 46. *Initial Reports of the Deep Sea*
31 901 *Drilling Project* **46**, 115–141.
- 32
33
34 902 Schmidt, M. (1996). Experimental constraints on recycling of potassium from subducted
35 903 oceanic crust. *Science* **272**, 1927–1930.
- 36
37
38 904 Schmidt, M. W. & Poli, S. (1998). Experimentally based water budgets for dehydrating slabs
39 905 and consequences for arc magma generation. *Earth and Planetary Science Letters*
40 906 **163**, 361–379.
- 41
42
43 907 Schmidt, M. W. & Poli, S. (2014). Devolatilization During Subduction. In: Rudnick, R. L.
44 908 (ed.) *Treatise on Geochemistry (Second Edition)* **4**, 669-701.
- 45
46 909 Schmidt, M. W., Vielzeuf, D. & Auzanneau, E. (2004). Melting and dissolution of
47 910 subducting crust at high pressures: the key role of white mica. *Earth and Planetary*
48 911 *Science Letters* **228**, 65–84.
- 49
50
51 912 Seyfried, W., Berndt, M. & Seewald, J. (1988). Hydrothermal alteration processes at mid-
52 913 ocean ridges: constraints from diabase alteration experiments, hot spring fluids and
53 914 composition of the oceanic. *The Canadian Mineralogist* **26**, 787–804.
- 54
55
56
57
58
59
60

- 1
2
3 915 Skora, S. & Blundy, J. (2010). High-pressure Hydrous Phase Relations of Radiolarian Clay
4 916 and Implications for the Involvement of Subducted Sediment in Arc Magmatism.
5 917 *Journal of Petrology* **51**, 2211–2243.
- 6
7
8 918 Skora, S. & Blundy, J. (2012). Monazite solubility in hydrous silicic melts at high pressure
9 919 conditions relevant to subduction zone metamorphism. *Earth and Planetary Science*
10 920 *Letters* **321-322**, 104–114.
- 11
12
13 921 Spandler, C., Hermann, J., Arculus, R. & Mavrogenes, J. (2003). Redistribution of trace
14 922 elements during prograde metamorphism from lawsonite blueschist to eclogite facies;
15 923 implications for deep subduction-zone processes. *Contributions to Mineralogy and*
16 924 *Petrology* **146**, 205–222.
- 17
18
19 925 Spandler, C. & Pirard, C. (2013). Element recycling from subducting slabs to arc crust: A
20 926 review. *Lithos* **170-171**, 208–223.
- 21
22
23 927 Staudigel, H., Hart, S. & Richardson, S. (1981a). Alteration of the oceanic crust: processes
24 928 and timing. *Earth and Planetary Science Letters* **52**, 311–327.
- 25
26 929 Staudigel, H., Muehlenbachs, K., Richardson, S. H. & Hart, S. R. (1981b). Agents of low
27 930 temperature ocean crust alteration. *Contributions to Mineralogy and Petrology* **77**,
28 931 150–157.
- 29
30
31 932 Staudigel, H. & Plank, T. (1996). Geochemical fluxes during seafloor alteration of the
32 933 basaltic upper oceanic crust: DSDP Sites 417 and 418. In: Bebout, E., Scholl, W. &
33 934 Al., E. (eds.) *Geophysical Monograph Series 96*. AGU, 19–38.
- 34
35
36 935 Stolper, E. & Newman, S. (1994). The role of water in the petrogenesis of Mariana trough
37 936 magmas. *Earth and Planetary Science Letters* **121**, 293–325.
- 38
39 937 Sun, S.-S. & McDonough, W. F. (1989). Chemical and isotopic systematics of oceanic
40 938 basalts: implications for mantle composition and processes. *Geological Society,*
41 939 *London, Special Publications* **42**, 313–345.
- 42
43
44 940 Syracuse, E. M. & Abers, G. A. (2006). Global compilation of variations in slab depth
45 941 beneath arc volcanoes and implications. *Geochemistry, Geophysics, Geosystems* **7**,
46 942 1–18.
- 47
48
49 943 Syracuse, E. M., van Keken, P. E. & Abers, G. A. (2010). The global range of subduction
50 944 zone thermal models. *Physics of the Earth and Planetary Interiors* **183**, 73–90.
- 51
52 945 Thompson, G. (1983). Basalt-Seawater Interaction. In: Rona, P. A., Boström, K., Laubier, L.
53 946 & Smith, K. L. (eds.) *Hydrothermal Processes at Seafloor Spreading Centers: NATO*
54 947 *Conference Series IV: Marine Sciences 12P*, 225–278.
- 55
56
57
58
59
60

- 1
2
3 948 Tribuzio, R., Messiga, B., Vannucci, R. & Bottazzi, P. (1996). Rare earth element
4 949 redistribution during high-pressure–low-temperature metamorphism in ophiolitic Fe-
5 950 gabbros (Liguria, northwestern Italy): Implications for light REE. *Geology* **24**, 711–
6 951 714.
- 7
8
9 952 Truckenbrodt, J., Ziegenbein, D. & Johannes, W. (1997). Redox conditions in piston
10 953 cylinder apparatus: The different behavior of boron nitride and unfired pyrophanite
11 954 assemblies. *American Mineralogist* **82**, 337–344.
- 12
13
14 955 Ulmer, P. & Trommsdorff, V. (1995). Serpentine stability to mantle depths and subduction-
15 956 related magmatism. *Science* **268**, 858–61.
- 16
17
18 957 Van Keken, P. E., Hacker, B. R., Syracuse, E. M. & Abers, G. A. (2011). Subduction
19 958 factory: 4. Depth-dependent flux of H₂O from subducting slabs worldwide. *Journal*
20 959 *of Geophysical Research* **116**, 1–15.
- 21
22 960 Van Keken, P. E., Kiefer, B. & Peacock, S. M. (2002). High-resolution models of
23 961 subduction zones: Implications for mineral dehydration reactions and the transport of
24 962 water into the deep mantle. *Geochemistry, Geophysics, Geosystems* **3**, 1–20.
- 25
26
27 963 Yasuda, A., Fujii, T. & Kurita, K. (1994). Melting phase relations of an anhydrous mid-
28 964 ocean ridge basalt from 3 to 20 GPa: Implications for the behavior of subducted
29 965 oceanic crust in the mantle. *Journal of Geophysical Research* **99**, 9401–9414.

30
31
32 966
33
34 967 **FIGURE CAPTIONS**

35
36 968 *Figure 1:* Phase proportions in experiments on MORB and AOC (Table 2). Mineral
37
38 969 abbreviations are: grt=garnet; cpx=clinopyroxene; qtz/coe=quartz/coesite; ky=kyanite;
39
40 970 *=trace epidote, +=trace Fe-Ti oxide, ^=trace rutile.

41
42
43 971

44
45
46 972 *Figure 2:* Representative back-scattered electron (BSE) images of experimental run products
47
48 973 at different temperatures in MORB and AOC. Mineral abbreviations as in Fig. 1, plus
49
50 974 rt=rutile, vap=vapour and ep=epidote. Partial melts are always microvesicular due to
51
52 975 exsolution of water upon quench. In some experiments, we find clear evidence for the
53
54 976 presence of a vapour phase in addition to glass, as evidenced by a second, larger generation

1
2
3 977 of vesicles often containing “fish egg” textured spherules (quenched silicate fraction of a
4
5 978 fluid phase rich in dissolved silicates, *c.f.* Adam *et al.*, 1997).
6
7

8 979

9
10 980 *Figure 3:* (a) Al/(Na+K+2Ca) ratios of quenched glasses showing a trend from peraluminous
11
12 981 to metaluminous compositions at higher temperatures. (b) The granite classification scheme
13
14 982 of Barker (1979) indicating that the experimental partial melts are trondhjemitic to tonalitic
15
16 983 in composition.
17
18

19 984

20
21
22 985 *Figure 4:* Major element chemistry of quenched glasses (on an anhydrous basis) showing
23
24 986 systematic changes with temperature. Where SiO₂ decreases, Al₂O₃ systematically increases
25
26 987 with increasing temperature. The general tendency for CaO to increase with increasing
27
28 988 temperature is consistent with the progressive consumption of clinopyroxene and epidote
29
30 989 during melting. Titanium oxide contents increase systematically with increasing temperature
31
32 990 in the presence of rutile because of increasing solubility.
33
34

35 991

36
37
38 992 *Figure 5:* Trace element compositions of experimental glasses normalised to PUM (primitive
39
40 993 upper mantle; Sun & McDonough, 1989). Starting compositions are shown as thick solid
41
42 994 grey lines. At low temperatures trace element patterns are spiky, becoming smoother and
43
44 995 approaching their levels in the starting materials as temperature increases. Fluid-mobile
45
46 996 elements (e.g. alkalis) are the most enriched at all conditions. Light REE are strongly
47
48 997 depleted in partial melts, due to the presence of residual epidote up to ~900°C. Glasses also
49
50 998 show enrichment of Zr (over Nd), Hf (over Sm) and Li (over Y), although these
51
52
53
54
55
56
57
58
59
60

1
2
3 999 characteristics are rarely reflected in arc magmas because of the subsequent control exerted
4
5
6 1000 by mantle wedge peridotite.
7

8 1001

9
10 1002 *Figure 6:* Trace element chemistry of quenched glasses showing systematic changes with
11
12 1003 temperature. Different element groups behave differently with increasing temperature, e.g.
13
14 1004 HREE, Y and Sc concentrations increase with increasing temperature, in contrast to most
15
16 1005 fluid-mobile elements. The different trace element patterns can be related to the presence or
17
18 1006 absence of residual phases as well as the additional vapour.
19

20 1007

21
22 1008 *Figure 7:* Schematic subcritical silicate-H₂O diagram versus temperature at constant pressure
23
24 1009 (3 GPa) (after Manning, 2004). Note that this sketch does not attempt to illustrate the
25
26 1010 chemography of our bulk-rocks. Instead, the figure approximates melt-fluid equilibrium in a
27
28 1011 simplified case in which the bulk composition corresponds to the minimum melt (+ H₂O) of
29
30 1012 AOC and MORB. Different residual solid phases that are present in our experimental run
31
32 1013 products are ignored here. It is illustrated in the diagram that our experiments only constrain
33
34 1014 the temperature at which two fluids condense to a single fluid (solvus: dashed lines).
35
36 1015 However, the position along the abscissa is not constrained because we did not vary the
37
38 1016 experimental water content. It is therefore possible that two fluids would have been present
39
40 1017 at higher temperatures, had more water been added.
41
42 1018

43 1019

44 1020 *Figure 8:* Variation of log Σ LREE (La-Sm) in glasses *versus* temperature. Solid curves are
45
46 1021 modelled Σ LREE using the allanite solubility equation (9) given in Klimm *et al.* (2008), for
47
48 pure allanite ($X_{\text{all}}=1$), and for $X_{\text{all}}=0.3$ (approximating the composition found by Klimm *et*
49
50
51
52
53
54
55
56
57
58
59
60

1
2
3 1022 *al.*, 2008). The Σ LREE of our undoped experiments is significantly lower when compared to
4
5 1023 allanite-saturated experiments, because these elements are hosted in epidote.
6
7
8 1024
9
10 1025 *Figure 9.* (La/Sm)_{PUM} versus Ba/Th for mafic arc lavas worldwide (compilation of Elliott,
11
12 1026 2003). Superimposed are the chemical compositions of the experimental glasses of this
13
14 1027 study, as well as the sub-solidus experiments of Green & Adam (2003). Barium/Th ratios are
15
16 1028 highest in our melts at 800-850°C from an AOC source, where epidote is present (retaining
17
18 1029 Th) but phengite (retaining Ba) is absent. Conversely, at low, sub-solidus temperatures,
19
20 1030 residual phengite will retain Ba and reduce Ba/Th in the fluids. Thus elevated Ba/Th is
21
22 1031 favoured by a narrow temperature interval between phengite-out and epidote-out.
23
24
25
26
27
28
29
30
31
32
33
34
35
36
37
38
39
40
41
42
43
44
45
46
47
48
49
50
51
52
53
54
55
56
57
58
59
60

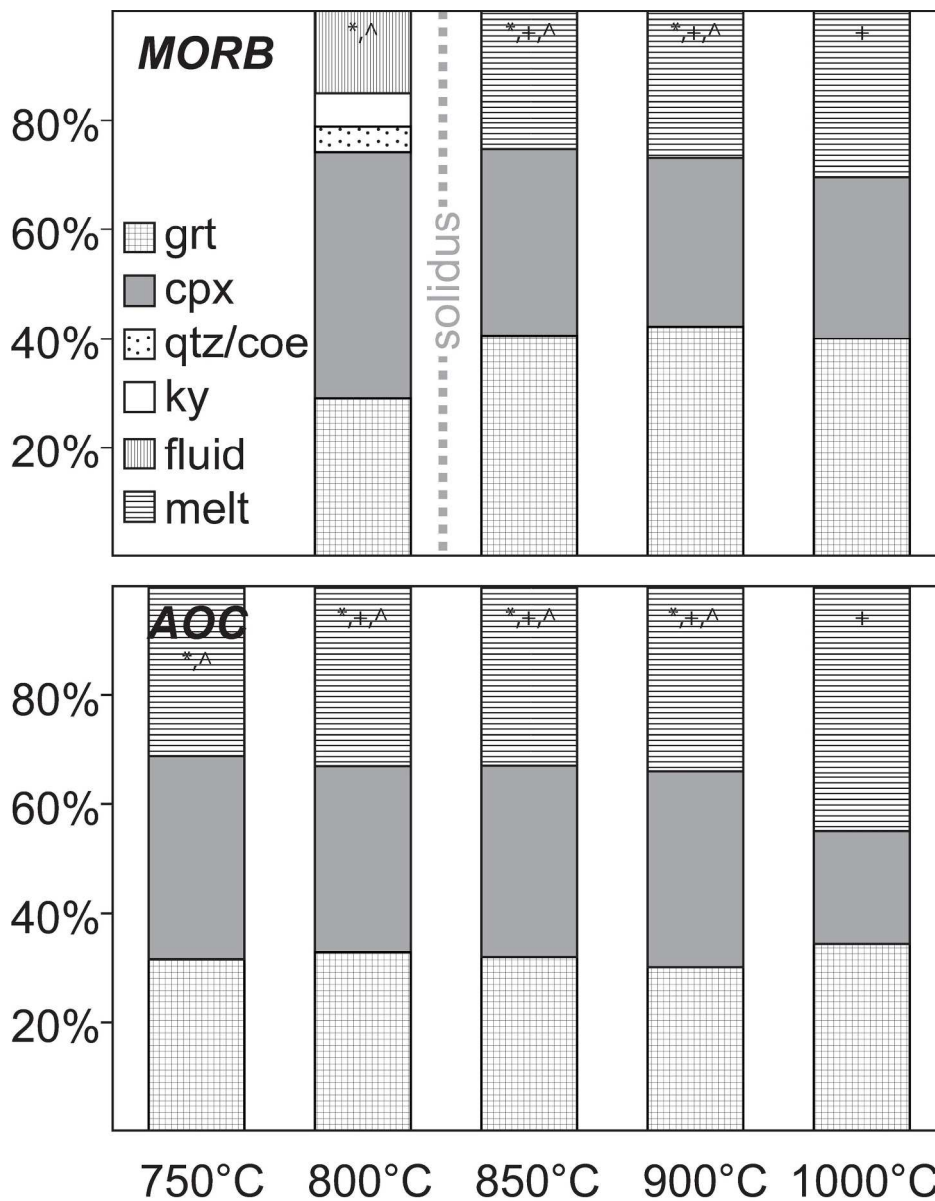


Figure 1
197x254mm (300 x 300 DPI)

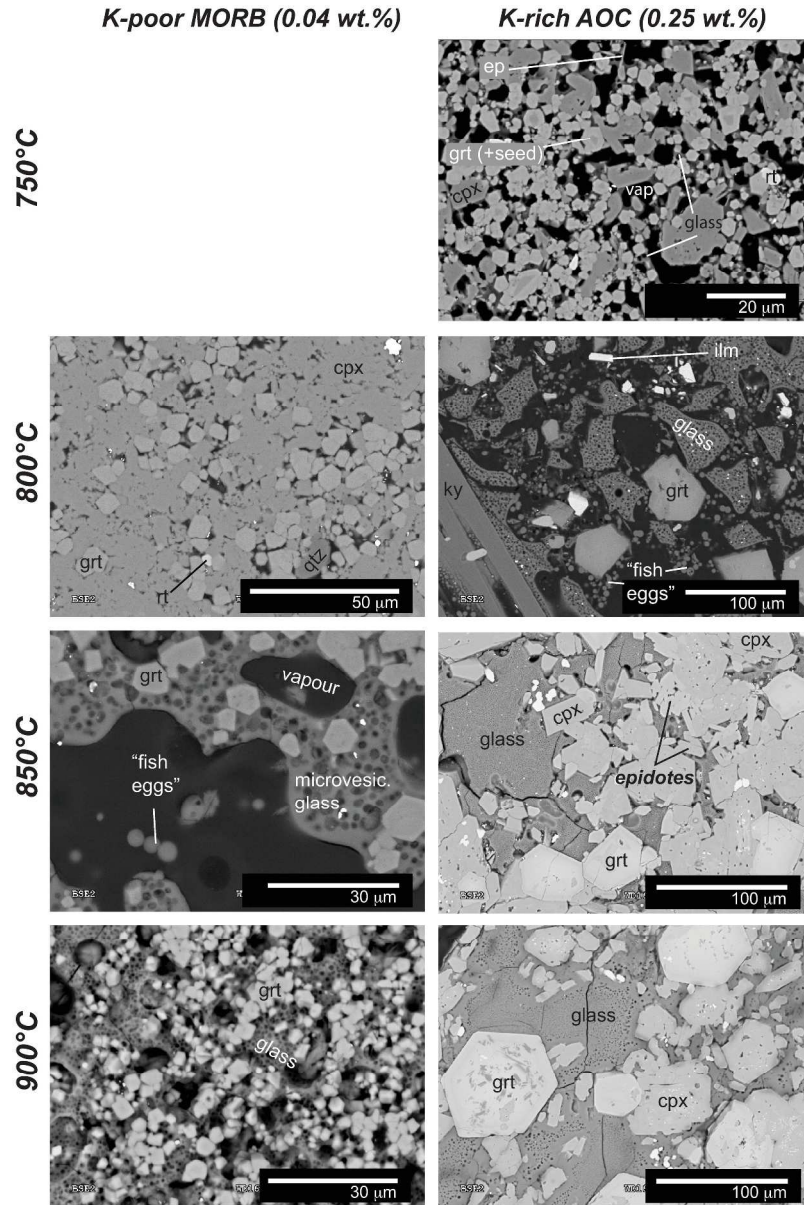


Figure 2
275x413mm (300 x 300 DPI)

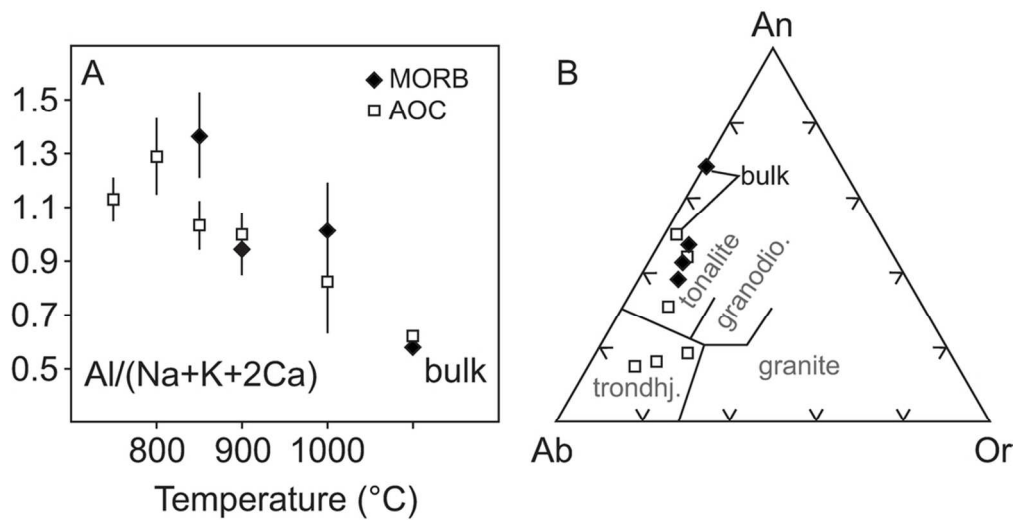


Figure 3
95x49mm (300 x 300 DPI)

Peer Review

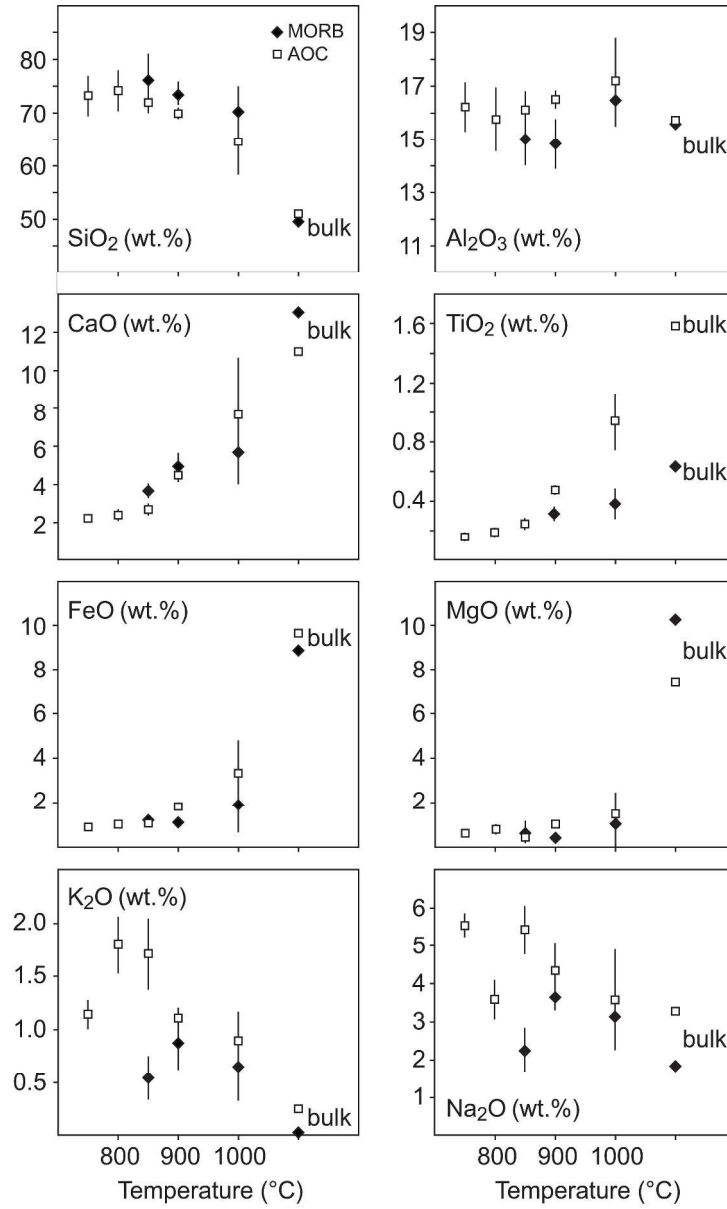


Figure 4
315x524mm (300 x 300 DPI)

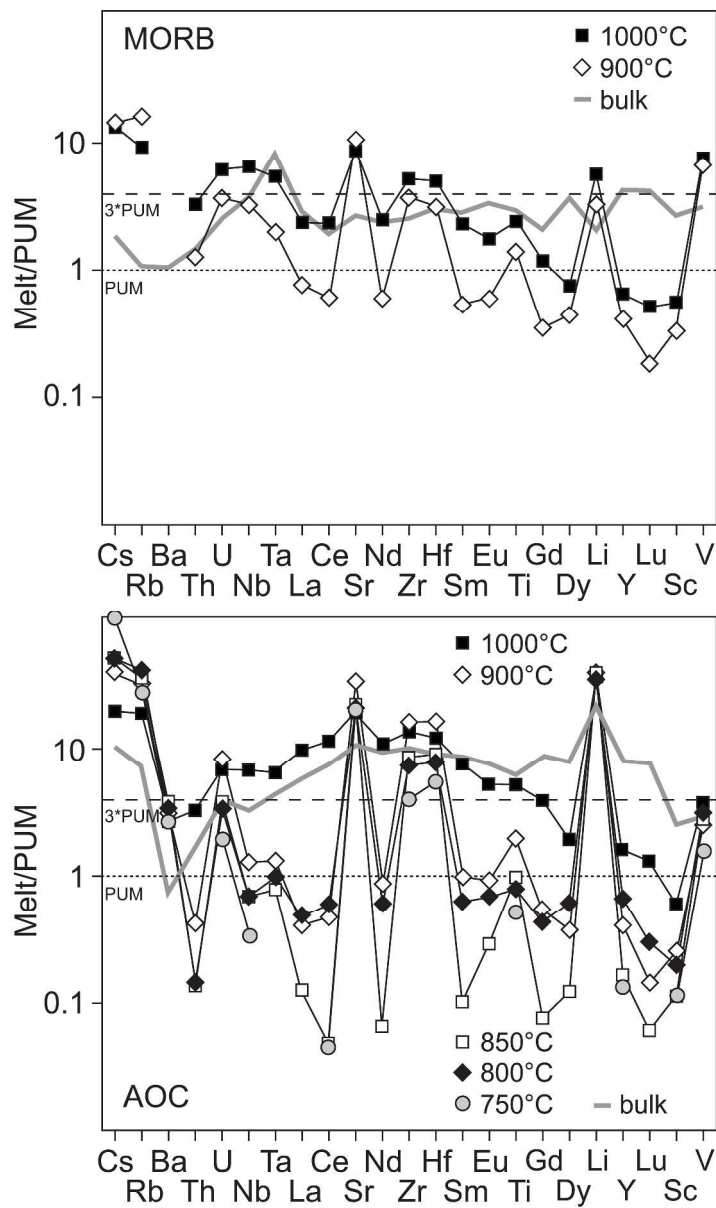


Figure 5
290x492mm (300 x 300 DPI)

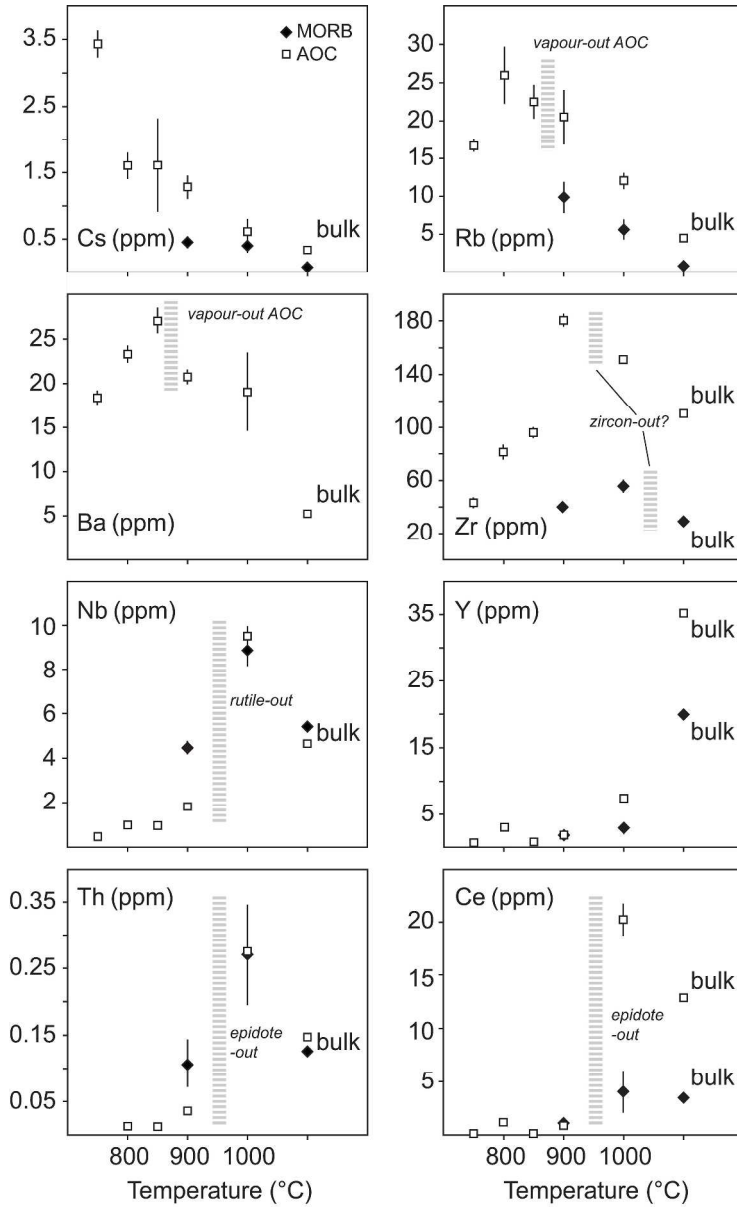


Figure 6
315x514mm (300 x 300 DPI)

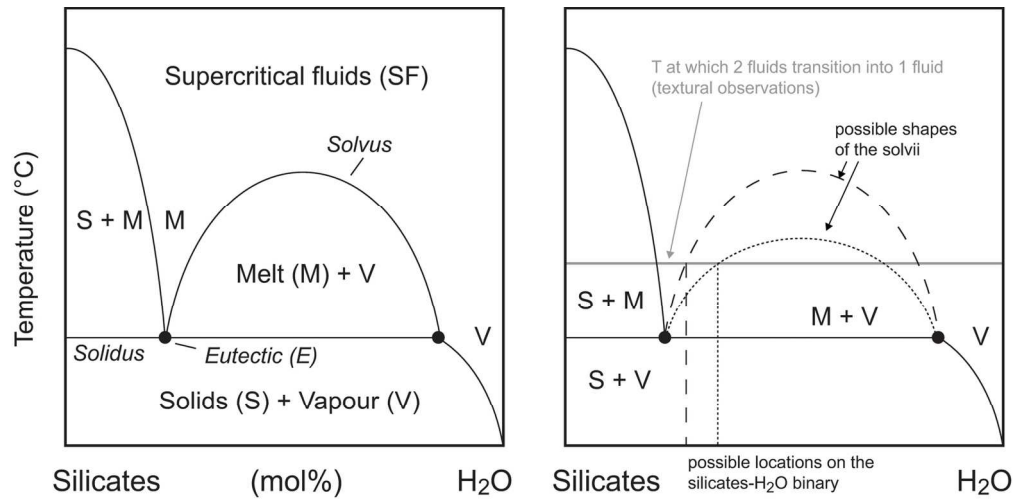


Fig.7
144x71mm (300 x 300 DPI)

Peer Review

1
2
3
4
5
6
7
8
9
10
11
12
13
14
15
16
17
18
19
20
21
22
23
24
25
26
27
28
29
30
31
32
33
34
35
36
37
38
39
40
41
42
43
44
45
46
47
48
49
50
51
52
53
54
55
56
57
58
59
60

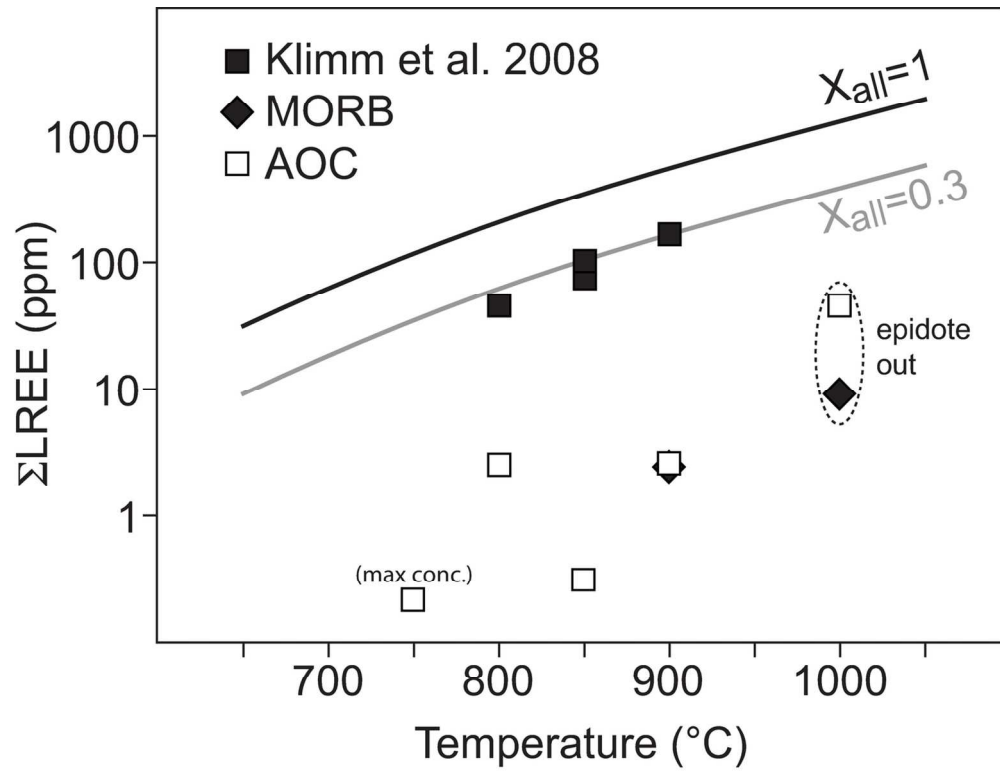


Fig.8
130x99mm (300 x 300 DPI)

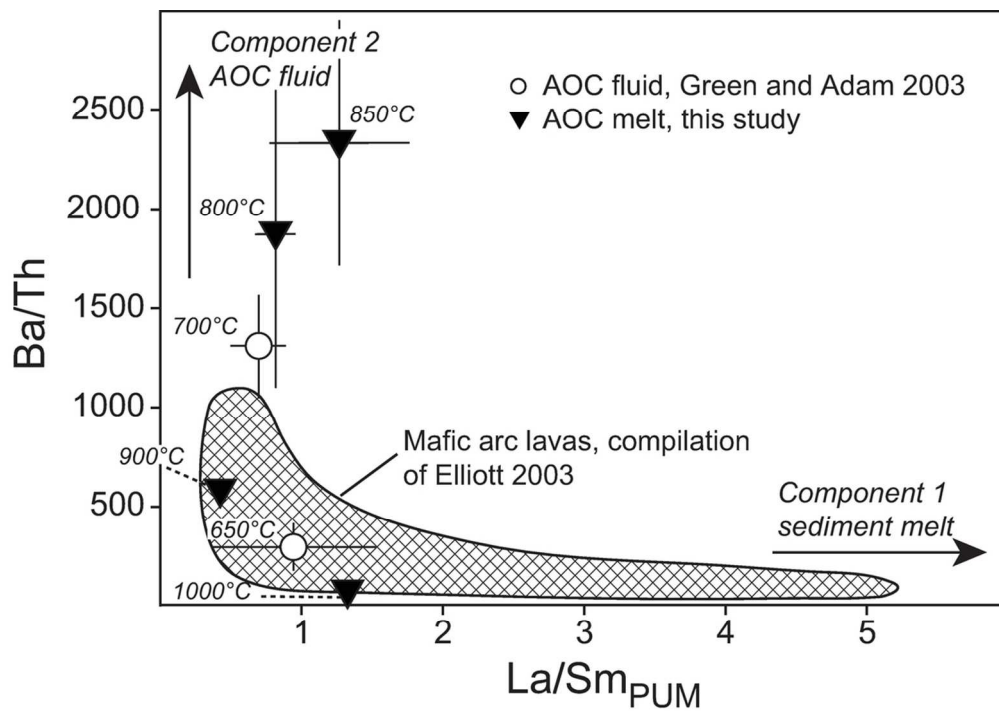


Figure 9
106x75mm (300 x 300 DPI)

Review

1
2
3
4
5
6
7
8
9
10
11
12
13
14
15
16
17
18
19
20
21
22
23
24
25
26
27
28
29
30
31
32
33
34
35
36
37
38
39
40
41
42
43
44
45
46
47
48
49
50
51
52
53
54
55
56
57
58
59
60

Table 1. Starting compositions of basalts used in various experiments (TS=this study, Kessel 05a/b, Klimm08, G&A03), in comparison to natural compositions (Devey94, Hoff88, LEG-46, Kelley03)

Comp. Study	"Pristine" MORB					"Altered" MORB (AOC)							
	TS	TS	Dev94	Kess05a	Kess05b	TS	TS	LEG46	LEG46	Kelley03	Klimm08	G&A03	Hoff88
Type	MORB	Stdev	37DS-1	*Syn. MORB	Syn. MORB	AOC	Stdev	A3-Av	Stdev	Av. AOC Pacific	*Syn. AOC	*Oc. Tholeiite	Av. MORB
Majors (wt.%)													
n	20	20	1	-	-	40	40	12	12	117	-	-	26
SiO ₂	49.6	0.3	48.7	53.4	51.7	51.0	0.5	50.5	0.3	50.4	50.0	51.3	50.7
TiO ₂	0.63	0.02	0.64	1.45	1.52	1.58	0.04	1.66	0.02	1.74	1.17	1.89	1.62
Al ₂ O ₃	15.5	0.1	15.9	17.2	16.7	15.7	0.3	15.5	0.2	12.3	16.1	14.1	15.3
FeO _{tot}	8.9	0.2	10.1	8.50	9.98	9.6	0.2	10.0	0.2	12.5	11.7	12.2	10.5
MnO	0.18	0.04	0.18	-	-	0.13	0.03	0.20	0.01	0.23	0.10	0.19	-
MgO	10.3	0.1	10.1	5.93	7.03	7.4	0.1	7.7	0.3	6.36	7.16	6.55	7.62
CaO	13.0	0.1	12.7	10.2	9.92	11.0	0.1	10.9	0.1	13.3	10.2	10.5	11.4
Na ₂ O	1.83	0.08	1.71	3.24	3.17	3.3	0.1	3.0	0.1	2.35	3.31	2.80	2.69
K ₂ O	0.04	0.01	0.03	-	-	0.25	0.02	0.21	0.08	0.63	0.28	0.31	0.11
P ₂ O ₅	0.05	0.02	0.04	-	-	ND	ND	0.14	0.01	0.17	-	0.22	-
Sum	100	-	100	100	100	100	-	100	-	100	100	100	100
Mg#	0.67	0.01	0.64	0.55	0.56	0.58	0.01	0.58	0.01	0.48	0.52	0.49	0.56
Traces (ppm)													
n	5	5	1	-	-	5	5	4-12	4-12	117	-	-	26
Li	3.39	0.07	-	247	-	33.3	0.1	13	12	14.1	92	82.6	-
Sc	47	1	-	148	-	41.8	0.8	38	1	37.4	83	-	41.4
Ti	3880	60	-	8590	-	9034	248	9822	113	-	7010	11300	9740
V	265	6	-	-	-	233	4	282	5	338	48	355	-
Rb	0.7	0.2	0.58	84	-	4.4	0.5	1.9	1.1	13.7	-	102	1.26
Sr	56	1	55	113	-	214	3	137	5	109	36	210	113
Y	19.8	0.3	18.6	102	-	34	1	34.8	1.1	40.7	40	159	35.8

1														
2														
3														
4	Zr	29.2	0.5	28	151	-	107	6	116	3	112	145	227	104
5	Nb	2.7	0.2	1.69	135	-	2.3	0.2	1.9	0.4	2.89	120	128	3.51
6	Cs	0.06	0.03	-	87	-	0.32	0.07	-	-	0.317	-	80.7	0.014
7	Ba	7.1	0.2	6.9	97	-	5.1	0.7	-	-	15.6	-	176	13.9
8	La	2.0	0.1	1.00	131	-	3.8	0.2	4.3	0.4	3.4	158	97.0	3.90
9	Ce	3.4	0.2	2.91	137	-	13	1	11.8	1.5	11.4	167	114	12.0
10	Nd	3.2	0.3	3.22	176	-	13	1	10.6	1.1	11.3	176	-	11.2
11	Sm	1.3	0.1	1.33	180	-	3.7	0.3	4.1	0.2	3.95	163	94.3	3.75
12	Eu	0.57	0.07	0.57	192	-	1.2	0.1	1.32	0.02	1.34	207	-	1.34
13	Gd	1.26	0.09	2.05	220	-	4.9	0.4	-	-	5.55	-	-	5.08
14	Dy	2.7	0.2	3.05	239	-	5.5	0.5	6.5	0.2	6.56	-	-	6.30
15	Lu	0.31	0.04	0.35	143	-	0.55	0.03	0.64	0.03	0.636	133	100	0.589
16	Hf	0.9	0.2	1.04	231	-	2.6	0.3	3.0	0.1	3.07	39	13.5	2.97
17	Ta	0.34	0.02	-	120	-	0.17	0.03	0.20	0.01	0.21	36	11.2	0.192
18	Th	0.13	0.01	-	229	-	0.14	0.03	0.15	0.01	0.173	268	106	0.187
19	U	0.06	0.03	-	241	-	0.08	0.02	-	-	0.390	257	102	0.071
20														
21														
22														
23														
24														
25	ΣLREE	9.9	0.4	8.5	624	-	33	2	31	2	30	664	305	31

Major element analyses are recalculated on an anhydrous basis for comparison; trace element are given as published

- either not reported or not added to the experiment

Abbreviations used: Syn=synthetic; Av=average; Oc=oceanic; TS=this study; ND=not determined

* trace element doped compositions

LEG56-A3-Av: majors, Rb, Sr, Y, Zr, Nb: Dungan *et al.* (1979); Ti, V, Hf, Ta, Th: Bougault & Cambon (1979); Li, Sc, La, Ce, Nd, Sm, Eu,

Dy, Lu: Emmermann & Puchelt (1979)

Hoff88=Hofmann (1988); Kess05a/b=Kessel *et al.* (2005a/b); Kelley03=Kelley *et al.* (2003); Klimm08=Klimm *et al.* (2008); G&A03=Green & Adam (2003); Dev94=Devey *et al.* (1994).

Table 2. Run conditions and phase proportions

<i>P=3 GPa</i>	time	Temp.	major phases in %									
Run	[days]	[°C]	grt	cpx	qtz/coe	(st*)/ky	Fe-Ti	phen	liq	vapour	glass	trace phases
MORB												
LC2	7	800	29.1	44.9	4.7	6.2	-	-	15.0	X+FE	-	ep, rt
			<i>34.3</i>	<i>52.9</i>	<i>5.5</i>	<i>7.3</i>	-	-	-			
LC1	5	850	40.7	33.9	-	-	-	-	25.3	X+FE	X	ep, Fe-Ti, rt
			<i>47.2</i>	<i>39.5</i>	-	-	-	-	<i>13.3</i>			
LC3B	4	900	42.5	30.7	-	-	-	-	26.9	X	X	ep, Fe-Ti, rt
			<i>49.2</i>	<i>35.5</i>	-	-	-	-	<i>15.3</i>			
LC4	3	1000	40.7	29.3	-	-	-	-	30.2	-	X	Fe-Ti
			<i>47.0</i>	<i>33.8</i>	-	-	-	-	<i>19.4</i>			
AOC												
LCA0	8	750	-	59.6	5.9	15.9	1.7	1.8	15.0	X+FE	-	ep, rt, apa
			-	<i>70.2</i>	<i>7.0</i>	<i>18.7</i>	<i>2.1</i>	<i>2.1</i>	-			
LCA0 rep [#]	8	750	31.5	37.4	-	-	-	-	31.1	X	X	ep, rt, grt seeds
			<i>36.3</i>	<i>43.1</i>	-	-	-	-	<i>20.6</i>			
LCA2B	7	800	32.7	34.3	-	-	-	-	33.0	X+FE	X	ep, rt, Fe-Ti, ky
			<i>37.6</i>	<i>39.5</i>	-	-	-	-	<i>22.9</i>			
LCA1	5	850	31.8	35.4	-	-	-	-	32.7	(X)	X	ep, rt, Fe-Ti, ky
			<i>36.6</i>	<i>40.8</i>	-	-	-	-	<i>22.7</i>			
LCA3	4	900	30.3	35.7	-	-	-	-	34.0	-	X	ep, rt, Fe-Ti, ky
			<i>34.8</i>	<i>40.9</i>	-	-	-	-	<i>24.3</i>			
LCA4	3	1000	34.3	20.7	-	-	-	-	45.1	-	X	Fe-Ti
			<i>38.8</i>	<i>23.4</i>	-	-	-	-	<i>37.8</i>			

[#]LCA0 rep is a repeat experiment of LCA0, run with grt seeds at ETH Zürich, see Methods for more information

Abbreviations used: grt=garnet; cpx=clinopyroxene; qtz/coe=quartz/coesite; ky=kyanite; Fe-Ti=Fe-Ti oxide; phen=phengite; liq=bulk liquid; ep=epidote; rt=rutile; apa=apatite; FE="fish eggs"; (st*) refers to the presence of staurolite as Al-rich phase in AOC sub-solidus experiment .

Mass balances were initially performed using anhydrous compositions (values in italic), and H₂O was later reintegrated (see text)

Table 3. Major and minor element compositions of experimental glasses

Exp. Type	LC1 measured	LC1 SD	LC1 anhydr.	LC3B measured	LC3B SD	LC3B anhydr.	LC4 measured	LC4 SD	LC4 anhydr.	LCA0 rep measured	LCA0 rep SD	LCA0 rep anhydr.
T (°C)	850	850	850	900	900	900	1000	1000	1000	750	750	750
(wt %)	<i>MORB</i>	<i>MORB</i>	<i>MORB</i>	<i>MORB</i>	<i>MORB</i>	<i>MORB</i>	<i>MORB</i>	<i>MORB</i>	<i>MORB</i>	<i>AOC</i>	<i>AOC</i>	<i>AOC</i>
n	24	24	24	36	36	36	52	52	52	8	8	8
SiO₂	60	4	76	57	2	74	54	3	71	58	3	73
TiO₂	0.19	0.03	0.24	0.25	0.04	0.32	0.29	0.08	0.38	0.12	0.02	0.15
Al₂O₃	11.9	0.8	15.0	11.5	0.7	14.8	12.6	0.8	16.4	12.8	0.7	16.2
FeO_{tot}	0.9	0.2	1.2	0.9	0.1	1.1	1.5	0.9	1.9	0.7	0.1	0.8
MgO	0.5	0.4	0.7	0.3	0.1	0.4	1	1	1	0.5	0.1	0.6
CaO	2.9	0.3	3.7	3.8	0.6	4.9	4	1	6	1.7	0.2	2.2
Na₂O	1.8	0.5	2.3	2.8	0.3	3.6	2.4	0.7	3.1	4.4	0.2	5.5
K₂O	0.4	0.2	0.5	0.7	0.2	0.9	0.5	0.3	0.7	0.9	0.1	1.1
P₂O₅	0.2	0.1	0.2	0.2	0.1	0.3	0.1	0.1	0.1	0.11	0.04	0.14
Sum	79	5	100	78	2	100	77	3	100	79	4	100
Al/(K+Na+2Ca)	1.4	0.2	1.4	0.9	0.1	0.9	1.0	0.2	1.0	1.1	0.1	1.1
(Na+K)/Al	0.29	0.07	0.29	0.47	0.05	0.47	0.36	0.09	0.36	0.64	0.06	0.64
Mg#	0.5	0.4	0.5	0.4	0.2	0.4	0.5	0.8	0.5	0.6	0.2	0.6

Exp. Type T (°C)	LCA2B measured 800	LCA2B SD 800	LCA2B anhydr. 800	LCA1 measured 850	LCA1 SD 850	LCA1 anhydr. 850	LCA3 measured 900	LCA3 SD 900	LCA3 anhydr. 900	LCA4 measured 1000	LCA4 SD 1000	LCA4 anhydr. 1000
(wt %)	<i>AOC</i>	<i>AOC</i>	<i>AOC</i>	<i>AOC</i>	<i>AOC</i>	<i>AOC</i>	<i>AOC</i>	<i>AOC</i>	<i>AOC</i>	<i>AOC</i>	<i>AOC</i>	<i>AOC</i>
n	46	46	46	34	34	34	36	36	36	44	44	44
SiO₂	59	3	74	61	2	72	61	1	70	54	5	65
TiO₂	0.15	0.02	0.19	0.21	0.03	0.25	0.41	0.03	0.47	0.8	0.2	0.9
Al₂O₃	12.5	0.9	15.7	13.6	0.6	16.1	14.3	0.3	16.5	14	1	17
FeO tot	0.8	0.1	1.0	0.9	0.2	1.1	1.6	0.1	1.8	3	1	3
MgO	0.6	0.2	0.8	0.3	0.2	0.4	0.9	0.1	1.0	1.3	0.8	1.5
CaO	1.9	0.2	2.4	2.3	0.3	2.7	3.9	0.3	4.5	6	3	8
Na₂O	2.8	0.4	3.6	4.6	0.5	5.4	3.8	0.6	4.3	3	1	4
K₂O	1.4	0.2	1.8	1.4	0.3	1.7	0.96	0.08	1.11	0.7	0.2	0.9
P₂O₅	0.31	0.08	0.39	0.32	0.07	0.38	0.36	0.06	0.42	0.2	0.1	0.3
Sum	80	4	100	84	2	100	86.7	0.9	100.0	84	4	100
Al/(K+Na+2Ca)	1.3	0.1	1.3	1.0	0.1	1.0	1.0	0.1	1.0	0.8	0.2	0.8
(Na+K)/Al	0.50	0.07	0.50	0.67	0.08	0.67	0.51	0.07	0.51	0.4	0.1	0.4
Mg#	0.6	0.2	0.6	0.4	0.2	0.4	0.5	0.1	0.5	0.4	0.3	0.4

SD=refers to 1 sigma of n (number) analyses; anhydr.=anhydrous

Table 4. Major and minor element composition of "fish eggs".

Exp. Type T (°C)	LC1 measured 850	LC1 SD 850	LC1 anhydr. 850	LCA2B measured 800	LCA2B SD 800	LCA2B anhydr. 800
(wt.%)	<i>MORB</i>	<i>MORB</i>	<i>MORB</i>	<i>AOC</i>	<i>AOC</i>	<i>AOC</i>
n	7	7	7	13	13	13
SiO₂	65	5	81	65	2	78
TiO₂	0.15	0.07	0.19	0.11	0.04	0.13
Al₂O₃	11	1	13	13	1	15
FeO tot	0.7	0.3	0.8	0.4	0.1	0.5
MgO	0.4	0.2	0.5	0.4	0.3	0.4
CaO	2.5	0.4	3.1	1.8	0.4	2.2
Na₂O	0.5	0.3	0.6	1.6	0.5	1.9
K₂O	0.31	0.03	0.39	1.2	0.3	1.4
P₂O₅	0.05	0.03	0.06	0.15	0.05	0.18
Sum	80	6	100	83	2	100

SD=refers to 1 sigma of n (number) analyses; anhydr.=anhydrous

Table 5. Trace element compositions of hydrous glasses

Exp. Type T (°C)	LC3B	LC3B	LC4	LC4	LCA0*	LCA0*	LCA2B	LCA2B	LCA1	LCA1	LCA3	LCA3	LCA4	LCA4
	meas	stdev	meas	stdev	rep meas	rep stdev	meas	stdev	meas	stdev	meas	stdev	meas	stdev
(ppm)	900	900	1000	1000	750	750	800	800	850	850	900	900	1000	1000
	<i>MORB</i>	<i>MORB</i>	<i>MORB</i>	<i>MORB</i>	<i>AOC</i>	<i>AOC</i>	<i>AOC</i>	<i>AOC</i>	<i>AOC</i>	<i>AOC</i>	<i>AOC</i>	<i>AOC</i>	<i>AOC</i>	<i>AOC</i>
n	7	7	5	5	11	11	5	5	5	5	5	5	6	6
Li	5.1	0.8	9	2	-	-	38	7	63	9	65	3	58	6
Sc	5.6	0.4	10	2	1.9	0.3	3.4	0.3	1.9	0.2	4.4	0.6	10.3	0.6
Ti	1770	50	3040	420	655	31	1020	150	1270	140	2580	60	7000	340
V	530	40	600	150	131	9	260	20	230	20	209	5	310	30
Rb	10	2	6	1	16.7	0.9	26	4	23	2	20	4	12	1
Sr	220	10	180	60	415	12	440	20	470	10	720	30	400	20
Y	1.9	0.2	2.9	0.9	0.60	0.05	3.0	0.4	0.75	0.06	1.9	0.1	7.4	0.4
Zr	40.3	0.9	56	5	43	2	81	6	96	3	181	5	151	4
Nb	2.2	0.1	4.4	0.3	0.24	0.03	0.50	0.09	0.49	0.06	0.92	0.06	4.8	0.2
Cs	0.4	0.1	0.4	0.1	3.4	0.2	1.6	0.2	1.6	0.7	1.3	0.2	0.6	0.2
Ba	-	-	-	-	18.4	0.8	23.3	0.9	27	1	20.7	0.8	19	4
La	0.52	0.06	1.6	0.8	<0.04	-	0.34	0.08	0.09	0.02	0.28	0.07	6.7	0.6
Ce	1.1	0.3	4	2	0.08	0.02	1.1	0.1	0.09	0.01	0.9	0.1	20	2
Nd	0.8	0.2	3	2	<0.02	-	0.8	0.1	0.09	0.06	1.2	0.2	15	2
Sm	0.24	0.08	1.0	0.6	<0.02	-	0.28	0.03	0.05	0.02	0.4	0.1	3.4	0.3
Eu	0.10	0.04	0.3	0.2	<0.06	-	0.12	0.06	0.05	0.04	0.16	0.03	0.89	0.05
Gd	0.21	0.03	0.7	0.3	<0.03	-	0.26	0.04	0.05	0.02	0.32	0.07	2.3	0.2
Dy	0.32	0.06	0.5	0.3	0.08	0.02	0.5	0.1	0.09	0.03	0.28	0.06	1.4	0.2
Lu	0.014	0.006	0.04	0.01	<0.02	-	0.022	0.004	<DL	<DL	0.011	0.004	0.10	0.02
Hf	0.9	0.2	1.5	0.2	1.6	0.2	2.4	0.2	2.8	0.3	5.1	0.4	3.7	0.3
Ta	0.08	0.01	0.22	0.05	<0.03	-	0.04	0.01	0.03	0.02	0.05	0.01	0.27	0.05
Th	0.11	0.04	0.27	0.08	<0.02	-	0.012	0.005	0.012	0.003	0.036	0.003	0.28	0.04
U	0.07	0.02	0.12	0.06	0.04	0.01	0.07	0.02	0.08	0.04	0.17	0.04	0.14	0.04

ΣLREE	2.6	0.4	10	3	<0.2	-	2.5	0.2	0.3	0.1	2.7	0.2	45	2
Ba/Th	460	180	130	40	>920	-	1870	770	2330	610	580	50	70	20
La/Sm_{PUM}	1.5	0.3	1.1	0.5	-	-	0.8	0.1	1.3	0.5	0.4	0.1	1.3	0.1
U/Th_n	2	1	1.0	0.8	>3.5	-	10	6	12	9	9	4	0.9	0.4

*Experiment analyzed by LA-ICP-MS, all other exp are analyzed by SIMS; Ba concentrations for AOC are LA-ICP-MS data, see methods for more details

ΣLREE=SUM (La-Sm); La/Sm_{PUM} are PUM normalized; U/Th_n are source normalized

Analyses below detection limits (DL) are reported as <DL.